University of Alberta

Detachment of Air Bubbles from Slit Microchannels with Shearing Flow

by

Byron Percy Blackmore

A thesis submitted to the Faculty of Graduate Studies and Research in partial fulfillment of the requirements for the degree of Master of Science

Department of Mechanical Engineering

Edmonton, Alberta

Spring, 2000

National Library of Canada
Acquisitions and Bibliographic Services
395 Wellington Street
Ottawa ON K1A 0N4
Canada

Bibliothèque nationale du Canada
Acquisitions et services bibliographiques
395, rue Wellington
Ottawa ON K1A 0N4
Canada

Your file Votre référence

Our file Notre référence

The author has granted a non-exclusive licence allowing the National Library of Canada to reproduce, loan, distribute or sell copies of this thesis in microform, paper or electronic formats.

L'auteur a accordé une licence non exclusive permettant à la Bibliothèque nationale du Canada de reproduire, prêter, distribuer ou vendre des copies de cette thèse sous la forme de microfiche/film, de reproduction sur papier ou sur format électronique.

The author retains ownership of the copyright in this thesis. Neither the thesis nor substantial extracts from it may be printed or otherwise reproduced without the author's permission.

L'auteur conserve la propriété du droit d'auteur qui protège cette thèse. Ni la thèse ni des extraits substantiels de celle-ci ne doivent être imprimés ou autrement reproduits sans son autorisation.

0-612-60103-X

Canada

University of Alberta

Library Release Form

Name of Author: Byron Percy Blackmore

Title of Thesis: Detachment of Air Bubbles from Slit Microchannels with Shearing Flow

Degree: Master of Science

Year this Degree Granted: 2000

Permission is hereby granted to the University of Alberta Library to reproduce single copies of this thesis and to lend or sell such copies for private, scholarly, or scientific research purposes only.

The author reserves all other publication and other rights in association with the copyright in the thesis, and except as hereinbefore provided, neither the thesis nor any substantial portion thereof may be printed or otherwise reproduced in any material form whatever without the author's prior written permission.

Byron Blackmore

Byron Percy Blackmore

205-10803 113th Street
Edmonton, Alberta
T5H 3J1

MARCH 1ST, 2000

University of Alberta

Faculty of Graduate Studies and Research

The undersigned certify that they have read, and recommend to the Faculty of Graduate Studies and Research for acceptance, a thesis entitled **Detachment of Air Bubbles from Slit Microchannels with Shearing Flow** submitted by Byron Percy Blackmore in partial fulfillment of the requirements for the degree of Master of Science.

Dr. D. Li

Dr. D. Dale

Dr. S. Liu

FEB. 28th, 2000

ABSTRACT

The flow velocity required to remove an air bubble attached to both surfaces of a slit microchannel was studied. The intent was to quantify the critical flow velocity in terms of bubble contact diameter, D_c, and channel of height, h. First, the critical velocity was determined experimentally. Microchannels ranging from 34-164 microns were constructed for this purpose. Bubbles of various diameters were generated within these channels and a base engine oil was used as the shearing fluid. The critical velocity was found to decrease linearly with both increasing D_c and decreasing h. Second, a model to predict the critical velocity was developed. By equating formulations for the drag force on a bubble to an approximation for the adhesion force, the critical velocity can be calculated. Comparison of model predictions to experimental results show that the model performs well for ratios of D_c/h greater than five.

ACKNOWLEDGMENTS

The author would like to thank Dr. D. Li for his guidance and supervision and the Natural Sciences and Engineering Research Council of Canada for providing postgraduate funding through a PGS A Scholarship.

TABLE OF CONTENTS

CHAPTER 1: INTRODUCTION 1
1.1 Motivation 1
1.2 Problem Description 2
1.3 Literature Review 3
1.4 Background Theory 4
1.4.1 Interfacial Phenomenon 4
1.4.1.1 Surfaces and Interfaces 4
1.4.1.2 Surface Tension 5
1.4.1.3 Interface Shape and the Laplace Equation of Capillarity 6
1.4.1.4 Equilibrium Contact Angle and Young's Equation 8
1.4.1.5 Dynamic Contact Angles 9
1.4.1.6 Adhesion Forces 11
1.4.1.7 Capillary Numbers 12
1.4.2 Fluid Dynamics 13
1.5 Research Objectives 14
References 19

CHAPTER 2: CRITICAL STATE DETERMINATION EXPERIMENTS 19
2.1 Apparatus 19
2.1.1 Experimental Overview 19
2.1.2 Computer Imaging System 20
2.1.3 Microchannels 21
2.1.4 Test Cell 23
2.1.5 Precision Pump 24
2.1.6 Pressure Transducer 24
2.1.7 Liquid and Air Properties 25
2.1.8 Miscellaneous Equipment 25
2.2 Experimental Procedure 26
2.2.1 Coating Apparatus and Procedure 26
2.2.2 Bubble Positioning and Adhesion 27
2.2.3 Flow Increment Procedure 29
2.3 Results and Discussion 31
2.3.1 Summary of Experiments Conducted 31
2.3.2 Two Phase Flow Considerations and Bubble Shrinkage 32
2.3.3 Critical State Results 34
2.3.3.1 Contact Angle Hysteresis 34
2.3.3.2 Critical States 35
2.3.3.3 Other Fluids and Repeatability 36
2.3.3.4 Explanation for Experimental Scatter 37
2.4 Physical Explanation for Observed Trends 38
2.5 Uncertainty Analysis 41
2.5.1 Pressure Measurements 41
2.5.2 Mass Flow Rate Measurements 42

2.5.3 Mass Flow Rate Increment 43
2.5.4 Bubble Contact Diameter Measurement 45
2.5.5 Channel Height Measurement 46
2.5.6 Error Propagation – Critical Capillary Number 46
2.5.7 Error Propagation – D_c/h 47
2.5.8 Conclusions regarding Experimental Data 47

CHAPTER 3: CONTACT ANGLE MEASUREMENTS 65
3.1 Motivation 65
3.2 Procedure and Equipment 66
3.3 Data Analysis 69
3.4 Results and Discussion 70
3.4.1 Advancing and Receding Contact Angles 70
3.4.2 Equilibrium Contact Angle 70
3.4.3 Comparison to Detachment Experiment Observations 72

CHAPTER 4: LAPLACE EQUATION OF CAPILLARITY 77
4.1 Motivation 77
4.2 Laplace Equation of Capillarity 78
4.3 Solution Technique 80
4.4 Results 82

CHAPTER 5: MODELING OF THE CRITICAL STATE 89
5.1 Fluid Shearing Force 89
5.1.1 Drag Force 1 – Underestimate 90
5.1.2 Drag Force 2 – Overestimate 92
5.2 Adhesion Force 98
5.3 Determination of the Critical State 104
5.3.1 Solution Technique 105
5.4 Model Results 106
5.4.1 Model Predictions and Experimental Data 106
5.4.2 Dynamic Advancing Air Contact Angle Estimation 109
5.5 Model Performance 109

CHAPTER 6: SUMMARY AND FUTURE WORK 116
6.1 Summary 116
6.2 Future Work 117

BIBLIOGRAPHY 119
APPENDIX A: COMPUTER PROGRAMS 121

LIST OF TABLES

Table 2.1 - Magnification factors for experimental microscope settings 49

Table 2.2 - Summary of experimental channel heights 49

Table 2.3 - Experimental fluid properties 49

Table 2.4 - Approximate average flow increments for each channel 49

Table 4.1 - Summary of percentage deviations from a linear interface assumption in terms of channel height 86

Table 4.2 - Summary of percentage deviations from a linear interface assumption in terms of bubble contact diameter 86

LIST OF FIGURES

Figure 1.1 – Side view of bubble inside microchannel 16

Figure 1.2 – Top view of bubble inside microchannel 16

Figure 1.3 – Diagram of a sessile drop 17

Figure 1.4 – Diagram of a sliding sessile drop 17

Figure 1.5 – Diagram of coordinates used to integrate for the adhesion force 18

Figure 2.1 – Apparatus block diagram 50

Figure 2.2 – Sketch of microchannel 50

Figure 2.3 – Sketch of test cell 51

Figure 2.4 – Sketch of coating apparatus 51

Figure 2.5 – Images taken of bubble during adhesion process 52

Figure 2.6 – Graph of bubble contact diameter versus experimental pressure drop 55

Figure 2.7 – Graph of bubble contact diameter versus time 56

Figure 2.8 – Sketch relating interface shadow to contact angle 57

Figure 2.9 – Images of experimental bubbles 58

Figure 2.10 – Graph of experimental data at critical state 58

Figure 2.11 – Graph of experimental with additives 59

Figure 2.12 – Summary of experimental bubble shapes for h=34 μm experiments 60

Figure 2.13 – Summary of experimental bubble shapes for h=60 μm experiments 61

Figure 2.14 – Summary of experimental bubble shapes for h=122 μm experiments 62

Figure 2.15 – Summary of experimental bubble shapes for h=164 μm experiments 63

Figure 2.16 – Graph of experimental data in terms of dimensional quantities 64

Figure 2.17 – Pressure calibration curve 64

Figure 3.1 – Contact angle measurement apparatus 74

Figure 3.2 – Image of bubble just prior to detaching 74

Figure 3.3 – Sketch of code algorithm 75

Figure 3.4 – Image of a bubble at equilibrium 75

Figure 3.5 – Geometry for contact angle from interface shadow derivation 76

Figure 4.1 – Geometry for solving Laplace Equation of Capillarity 87

Figure 4.2 – Interface Profile for h=122 μm 87

Figure 4.3 – Graph of linear deviation versus channel height 88

Figure 5.1 – Sketch of a sphere in Stokes flow 110

Figure 5.2 – Geometrical difference between experimental and ideal bubble 110

Figure 5.3 – Sketch of moving three phase line 111

Figure 5.4 – Solution of Cox's analysis for advancing and receding contact angles 111

Figure 5.5 – Model predictions for h=34 μm 112

Figure 5.6 – Model predictions for h=60 μm 112

Figure 5.7 – Model predictions for h=122 μm 113

Figure 5.8 – Model predictions for h=164 μm 113

Figure 5.9 – Sketch of physical bubble shape as D_c/h approaches unity 114

Figure 5.10 – Sketch of model bubble shape as D_c/h approaches unity 114

Figure 5.11 – Graph of best fit advancing contact angle 115

NOMENCLATURE

A	- Surface phase area
A_f	- Bubble frontal area
Ca	- Capillary number
Ca_{cr}	- Capillary number at critical state
D	- Diameter of sphere
D_c	- Bubble contact diameter
D_{large}	- Largest bubble diameter
F_a	- Adhesion force
F_d	- Drag force
g	- Gravitational acceleration
h	- Channel height
i	- Discretization index in x-direction
L	- Channel length
L_m	- Macroscopic length scale
m_2, m_1	- Mass measurements
N_i	- Bulk phase mole numbers
N_i^s	- Surface phase mole numbers
P_a, P_l	- Air and oil pressure
P_L, P_V	- Bulk phase pressures (liquid and vapor)
ΔP	- Pressure drop across channel
ΔP_{bubble}	- Pressure drop across bubble
Q	- Volumetric flow rate

Q'	- Volumetric flow rate per unit width
$Q_{parabolic}$	- Volumetric flow rate per unit width for a parabolic velocity profile
Q_{shear}	- Volumetric flow rate per unit width for a linear velocity profile
R_1, R_2	- Principle radii of curvature of a surface
R_c	- Bubble contact radius
S	- Bulk phase entropy (Chapter 1)
S	- Flow shear rate (Chapter 5)
S_{ave}	- Average shear rate
S^s	- Surface phase entropy
S_{total}	- Total entropy of a system
S_L, S_V, S_{LV}	- Phase entropies (liquid, vapor, and liquid-vapor interface)
S_{shear}	- Shear rate for a linear velocity profile
$S_{parabolic}$	- Average shear rate for a parabolic velocity profile
s	- Microscopic slip length
T	- Temperature
T_L, T_V, T_{LV}	- Phase temperatures (liquid, vapor, and liquid-vapor interface)
t	- Elapsed time
U	- Bulk phase internal energy
U^s	- Surface phase internal energy
U_{cr}	- Mean velocity at critical state
u	- Velocity in x-direction
U_m	- Mean velocity
U_{max}	- Maximum velocity in a parabolic velocity profile

u_i - Uncertainty in the quantity i

V_L, V_V - Bulk phase volume (liquid and vapor)

W - Channel width

W_1, W_2 - Weighting factors

x, y, z - Coordinates

Greek

β - Dummy variable

γ - Surface tension in oil-air interface

δ_a - Measure of interface curvature for the advancing dynamic contact angle

δ_r - Measure of interface curvature for the receding dynamic contact angle

ε_s - Microscopic slip length

η - Angular coordinate

θ_a, θ_r, θ_e - Contact angle (advancing, receding, and equilibrium)

θ' - Contact angle minus π

λ - Viscosity ratio

μ_i - Chemical potential

μ_{oil}, μ_{air} - Fluid viscosity (oil and air)

ρ_l, ρ_a - Fluid density (oil and air)

$\Delta\rho$ - Density difference

CHAPTER 1

INTRODUCTION

1.1 MOTIVATION

The behavior of three phase systems is important in numerous applications. Some industrial applications are enhanced oil recovery, filtration processes, mixing operations, adhesive design, or any process which involves two phase flow considerations. Three phase systems are prevalent in spraying and coating operations in which the movement of the three phase interface governs the systems performance. Understanding how interfacial physics affect these applications is thus a very important endeavor. One application in particular is the focus of this research. The problem originates from experiments conducted by Imperial Oil Limited.

Lubrication is heavily reliant upon the lubricating medium being able to completely wet the surfaces of interest. Imperfect lubrication will result in expedited mechanical wear and, in severe cases, the failure of a machine part. It has been observed, when the clearances between two surfaces to be lubricated decrease to the scale of micrometers, that difficulty arises in completely wetting the entirety of the surfaces. One possible explanation of this poor surface wetting is that a minute pocket of air becomes trapped between the surfaces. Generally, the non-wetting spots on a metal surface are hydrophobic patches formed in two ways: chemical modification via interactions with the impurities or polymer additives in the oil, or the adsorption of polymer impurities/additives in the oil forming a hydrophobic coating.

It is desirable to be able to remove such pockets of air by forcing the lubricating fluid through the clearances with sufficient velocity and pressure.

1.2 PROBLEM DESCRIPTION

As this problem arises from within a lubrication context, the clearances to be studied will be quite small(34 μm – 164 μm). The air bubbles in this work were large enough to span the entire clearance. The fluid was forced to flow around the bubble. A sketch of the problem is shown in Figure 1.1. The air bubble is trapped between the upper and lower surfaces of a channel. The channel height, h, is on the order of micrometers to be consistent with typical lubrication clearances. Figure 1.2 gives a top view of the problem. As can be seen, the liquid must flow around the stationary bubble. The flow around the bubble will cause a drag force on the bubble. This drag force is the means by which the bubble must be removed.

In Figure 1.1, it can be seen that the liquid-air interface forms an angle with the solid surface. This angle is known as a contact angle. Contact angles and other interfacial phenomenon will be discussed comprehensively in Section 1.4. When the bubble is subjected to an external force, the contact angles will deform. The deformation of the contact angles is known as contact angle hysteresis. The contact angle hysteresis along with the liquid-air surface tension is the source of the adhesion force which resists the drag force. The bubble will be detached once the drag force caused by the liquid flow can overcome the retaining adhesion force.

1.3 LITERATURE REVIEW

There are several publications that deal with removing adhered liquid drops from solid surfaces with a shearing flow. Experiments to determine the required shear rate to remove an alkane droplet adhered to a smooth glass slide were performed Mahe et al. (1988). In this experiment the alkane drops were removed with water as the shearing fluid. The drops in this experiment were attached to one surface only and were very small in comparison with the channel dimensions. Mahe et al.(1988) found that larger flow shear rates were required to remove droplets of small diameter. Basu et al. (1997) attempted to describe the results of Mahe et al. by equating approximations for the drag force and the adhesion force. This model performed with moderate success with a tendency to over predict the required flow shear rate. The difference between these studies and the present investigation is that the current work deals with bubbles that span the entire channel height. This provides an additional surface for the bubble to adhere to and produces a substantially different flow field about the bubble. For instance, the shearing fluid in the work of Mahe et al.(1988), could flow around or above the droplet, while in this study, the shearing fluid is forced to flow around the bubble. The effect of changing the channel height will also be investigated in the current work. The research in literature gives no consideration to the effect of the channel dimensions in which the droplet is adhered.

There has been much work done in removing solid particles from channels(Jen et al., 1996, Kuo et al., 1997, Xia et al., 1994). This situation is fundamentally different from removing a liquid drop or air bubble. A drop or bubble will deform to change its contact

angles when subjected to an external force. This has the effect of strengthening the adhesive bond to the surface. A solid particle has no such mechanism for adjusting its adhesive force.

1.4 BACKGROUND THEORY

In the following sections, several key interfacial and fluid dynamics concepts will be presented. First, the basics of interfacial physics will be given as they are very important to the understanding of the problem. Derivations for the Laplace Equation of Capillarity and Young's Equation will be presented along with definitions for equilibrium and dynamic contact angles, surface tension, and adhesive force. The parameters that affect the behavior of the dynamic contact angles will be explained. Secondly, an introduction to the assumptions behind and behavior of Poiseuille flow will be given. Poiseuille flow describes how pressure driven flow will behave in very narrow channels. Assuming that Poiseuille flow exists is important to the models derived in Chapter 5.

1.4.1 Interfacial Phenomenon

1.4.1.1 Surfaces and Interfaces

A surface/interface is the boundary between two heterogeneous bulk phases. A bulk phase may be either a solid, a liquid, or a vapor. It is important not to regard an interface as a simple boundary however. The interface will have a characteristic thickness with different properties from either of the bulk phases that surround it. The interface thickness is typically

on the order of several molecular diameters or several nanometers. An interface will always take the shape of a three-dimensional surface.

Similarly, a three phase interface is the boundary between three heterogeneous bulk phases. It physically takes the shape of a three-dimensional line.

1.4.1.2 Surface Tension

It is well known that droplets and bubbles have a tendency to form spherical shapes if not influenced by external factors. The reason for such behavior is that the interface is under a state of tensile stress. This surface tension is dependent upon the material composing the surrounding bulk phases and has units of force per length. An expression for the surface tension can be found starting with the fundamental equation for a simple bulk phase [Callen, 1985]:

$$U = U(S, V, N_1, N_2, \ldots, N_r) \tag{1.1}$$

where U, S, V, and N_i, represent the internal energy, entropy, volume, and mole numbers of the bulk phase respectively. The fundamental equation for a surface phase is quite similar:

$$U^s = U^s(S^s, A, N_1^s, N_2^s, \ldots, N_r^s) \tag{1.2}$$

where U^s, S^s, A, N_i^s represent the internal energy, entropy, area, and mole numbers for the surface. Rewriting Equation 1.2 in differential form gives:

$$dU^s = T\,dS^s + \gamma dA + \sum \mu_i\, dN_i^s \tag{1.3}$$

where T, γ, and μ_i represent the intensive properties of temperature, surface tension, and chemical potential. Keeping the surface entropy and surface mole numbers constant, the

surface tension is:

$$\gamma = \frac{\partial U^s}{\partial A}\Big|_{S^s, N_i^s} \tag{1.4}$$

Thus, surface tension is described mathematically as the internal energy per surface area of an interface. The surface tension always behaves in a manner that will minimize the surface area.

1.4.1.3 Interface Shape and the Laplace Equation of Capillarity

The shape that an interface takes is governed by the Laplace Equation of Capillarity. The Laplace Equation of Capillarity can be derived by considering a bubble inside a bulk liquid phase. The total entropy for such a system is:

$$S_{total} = S_L + S_V + S_{LV} \tag{1.5}$$

where the subscripts L, V, LV, indicate the bulk liquid phase, bulk vapor phase, and liquid-vapor surface phase. The differential form of Equation 1.5 is:

$$dS_{total} = dS_L + dS_V + dS_{LV} \tag{1.6}$$

Each term in Equation 1.6 can be substituted for with the appropriate expression from the differential form of the fundamental equation. In particular, for the bulk liquid phase differential entropy:

$$dS_L = \frac{dU_L}{T_L} + \frac{P_L}{T_L} dV_L - \sum \frac{\mu_{iL}}{T_L} dN_{iL} \tag{1.7}$$

and the expressions for the bulk vapor and interface phases are similar. Performing these substitutions and rearranging results in:

$$dS_{total} = \frac{dU_L}{T_L} + \frac{P_L}{T_L} dV_L - \sum \frac{\mu_{iL}}{T_L} dN_{iL}$$
$$+ \frac{dU_V}{T_V} + \frac{P_V}{T_V} dV_V - \sum \frac{\mu_{iV}}{T_V} dN_{iV} \quad (1.8)$$
$$+ \frac{dU_{LV}}{T_{LV}} + \frac{\gamma_{LV}}{T_{LV}} dA_{LV} - \sum \frac{\mu_{iLV}}{T_{LV}} dN_{iLV}$$

The system is constrained by the following relations: the sum of the internal energies of the phases must be a constant:

$$dU_L + dU_V + dU_{LV} = 0 \quad (1.9)$$

the sum of the mole numbers must remain a constant:

$$dN_{iL} + dN_{iV} + dN_{iLV} = 0 \quad (1.10)$$

and the total volume of the bulk liquid and vapor phases must be a constant:

$$dV_L + dV_V = 0 \quad (1.11)$$

Incorporation of Equation 1.9, Equation 1.10, and Equation 1.11 into Equation 1.8 results in:

$$dS_{total} = \left(\frac{1}{T_L} - \frac{1}{T_{LV}}\right) dU_L + \left(\frac{1}{T_V} - \frac{1}{T_{LV}}\right) dU_V$$
$$+ \left(\frac{P_L}{T_L} - \frac{P_V}{T_V} + \frac{\gamma}{T_{LV}} \frac{dA}{dV_L}\right) dV_L \quad (1.12)$$
$$- \sum \left(\frac{\mu_{iL}}{T_L} - \frac{\mu_{iLV}}{T_{LV}}\right) dN_{iL} - \sum \left(\frac{\mu_{iV}}{T_V} - \frac{\mu_{iLV}}{T_{LV}}\right) dN_{iV}$$

At equilibrium, the temperature and chemical potentials in all phases will be the same. Considering this and setting dS_{total} to zero allows Equation 1.12 to simplify to:

$$P_L - P_V = \gamma \frac{dA}{dV_L} \quad (1.13)$$

which is the well known Laplace Equation of Capillarity. The rate of change of surface area

with the bulk liquid phase volume can be interpreted as the mean curvature of the surface phase. In a more recognizable form, Equation 1.13 is:

$$P_2 - P_1 = \gamma\left(\frac{1}{R_1} + \frac{1}{R_2}\right) \tag{1.14}$$

where P_2, P_1, R_1, R_2, and γ are the pressure on the concave side of the interface(i.e., the pressure inside the droplet), pressure on the convex side of the interface, the principle radii of curvature of the interface and the surface tension respectively. If the interface is assumed to be spherical then both radii of curvature will be the same and Equation 1.14 simplifies again to:

$$\Delta P = \frac{2\gamma}{R} \tag{1.15}$$

where R is the radius of the spherical bubble.

To use Equation 1.14 to compute the interface shape for an arbitrary situation is a complex process. Later, in Chapter 4, the interface shape will be computed for the situation modeled in this study.

1.4.1.4 Equilibrium Contact Angle and Young's Equation

As mentioned briefly above, it is possible for an interface to form a contact angle with a solid phase. Consider a fluid-gas interface intersecting with a solid phase as shown in Figure 1.3. This geometry is known as a sessile drop. The angle of intersection between the liquid-solid interface and the liquid-vapor interface is known as the contact angle, θ. The three phase interface line is known as the contact perimeter. Depending upon the properties of the

bulk phases present, the value of θ can range from 0 to 180 degrees. Typically, sessile drops are formed with a liquid drop in air on a solid surface. In Figure 1.3, γ_{LV}, γ_{LS}, and γ_{VS}, represent the interfacial tensions present in the liquid-vapor, liquid-solid, and vapor-solid phases respectively. A simple horizontal force balance on the right side of the droplet results in:

$$\gamma_{VS} + \gamma_{LV} \cos\theta = \gamma_{LS} \tag{1.16}$$

and rearranging gives the classical Young's Equation:

$$\cos\theta = \frac{\gamma_{VS} - \gamma_{LS}}{\gamma_{LV}} \tag{1.17}$$

A more rigorous derivation of the general Young's Equation would include the effects of the three phase interface line tension. Equation 1.17 neglects this contribution. In most cases, the line tension is very small in comparison to the surface tensions and can be neglected without significant error.

It should be noted that although a sessile drop was used to depict the preceding force balance, the choice was arbitrary. The equilibrium contact angle is not dependent upon the interface shape. It depends only upon the surface tensions of the interfaces from which it is formed. For example, using a similar force balance, one can find the contact angle that a meniscus forms in a capillary tube. The equilibrium contact angle is thus a localized phenomenon.

1.4.1.5 Dynamic Contact Angles

In the previous section, the equilibrium contact angle was described. The dynamic

contact angle is a different phenomenon. The equilibrium contact angle, as its name implies, is the contact angle formed when the interfaces are not in motion and the entire system is at steady state. The dynamic contact angle is measured in the same way but when the interfaces are moving relative to one another. This is most commonly encountered with a liquid-gas or liquid-liquid interface moving over a stationary surface. A diagram of a sessile drop moving along a solid surface is given in Figure 1.4. The contact angles at the advancing edge and the retreating edge do not have the same value. The advancing edge contact angle is called the dynamic advancing contact angle, θ_a, and similarly the retreating edge contact angle is called the dynamic receding contact angle, θ_r. The difference between the dynamic contact angles is called the contact angle hysteresis.

The dynamic contact angles, like the equilibrium contact angle, have a dependence upon surface tensions. However, this is not the only governing factor. It is well known that the dynamic advancing and receding angles have a strong dependence upon the speed at which the interface moves over the solid interface(Hoffman, 1975, Ngan and Dussan, 1982). At zero velocity, the dynamic contact angles both must be equal to the equilibrium contact angle. As the velocity of the interface increases, the difference between the dynamic contact angles and the equilibrium contact angle increases. The dynamic advancing contact angle will always become larger (as measured from the liquid side as shown in Figure 1.4) than the equilibrium contact angle and the dynamic receding contact angle will always become smaller. Thus, the contact angle hysteresis is a function of interface velocity as well.

The work of Cox (Cox, 1986) dealing with liquid spreading showed that the dynamic contact angles are also dependent upon the ratio of a characteristic macroscopic length to a

microscopic slip length. According to Cox, in the immediate region of the three phase line, there exists a slip length of length, s. This means that instead of having zero velocity at the solid surface as per the norm in fluid mechanics analysis, there is a small region with a non zero fluid velocity at the surface. Cox uses this assumption to solve the two phase Stokes flow field about an advancing interface. A relationship between the slip length, s, and a problem specific macroscopic length scale and the dynamic contact angles was determined. This relation was shown to explain the data of Hoffman (Hoffman, 1975) very well. In subsequent work, (Gu and Li, 1998, Basu et al., 1996), the value of the slip length has been repeatedly found to range from 1-5 μm. What this means is that by varying the macroscopic length scale, the dynamic contact angles will be changed. A more rigorous explanation of Cox's method will be given in Chapter 5.

1.4.1.6 Adhesion Forces

The source of the adhesion force is the contact angle hysteresis. The force of adhesion is simply the integral of all the surface tensions about the entire three phase line in the horizontal direction. Considering again the sessile drop in Figure 1.4, the integral of γ_{LS} and γ_{VS} about the entire contact perimeter can be seen to be zero. The reason for this is that these surface tensions do not change in magnitude and they cancel out as they are summed about the contact perimeter. The contribution from γ_{LV} will not cancel out because the contact angle varies about the contact perimeter. The net force from the liquid-vapor surface tension acts in the direction opposite to the external force. The dynamic contact angle must vary from the dynamic advancing contact angle value to the dynamic receding contact angle

value along the perimeter in some manner. Mathematically, this relation for the adhesion force can be written as:

$$F_a = \int \cos\theta \cos\eta \, R \, d\eta \tag{1.18}$$

where η is the angle coordinate as shown in Figure 1.5. The dynamic contact angle about the perimeter is some function of η. There are several valid assumptions about the variation of the dynamic contact angle about the contact perimeter in the literature. These assumptions will be compared with observations about the experiment in Chapter 5 to select the most appropriate method.

1.4.1.7 Capillary Numbers

The Capillary number is a non-dimensional quantity comparing viscous forces to interfacial forces. This number will be used as the primary method of expressing the experimental data. The Capillary number is:

$$Ca = \frac{\mu U_m}{\gamma} \tag{1.19}$$

where μ, γ, and U_m are the viscosity, surface tension of the fluid-vapor interface, and mean velocity of the shearing fluid respectively. The Capillary number is then a non-dimensional velocity. The Capillary number can also be used as a measure of interface rigidity. For a small value of Ca, the interfacial forces will be dominant and the interface will not deflect much when subjected to viscous forces. It will be shown that the Capillary numbers in this study are sufficiently small to allow the assumption of a rigid interface to be made.

1.4.2 Fluid Dynamics

In this study, the shearing fluid will be pumped through very narrow channels. The assumption that Poiseuille flow exists will be made in many instances. The following section will describe what Poiseuille flow is, when it can be assumed, and its characteristics.

Consider steady state, fully developed flow through an infinitely wide channel of height h. Assuming there is only velocity in the x-direction, the momentum equation in the x-direction simplifies to [Shames, 1992]:

$$\mu_{fluid} \frac{\partial^2 u}{\partial y^2} = \frac{dP}{dx} \tag{1.20}$$

It is well known that the pressure gradient in this situation is a constant value [Shames, 1992]. Using this information to integrate Equation 1.20 for the velocity profile results in:

$$u(y) = \frac{1}{2\mu_{fluid}} \frac{dP}{dx} y(y - h) \tag{1.21}$$

So clearly the velocity profile is parabolic. Integrating the velocity profile over the channel height results in a flow rate per unit width of:

$$Q' = \frac{-h^3}{12\mu_{fluid}} \frac{dP}{dx} \tag{1.22}$$

and rearranging leads to a more familiar formulation:

$$\frac{dP}{dx} = \frac{-12Q\mu_{fluid}}{h^3} \tag{1.23}$$

The pressure gradient is inversely proportional to h^3. Thus, large pressure gradients can be expected in channels of small height. This information will be used to explain much of the

experimental data in Section 2.4.

Of course, infinitely wide channels cannot be created. It is important to know just how wide a channel must be in order to apply the Poiseuille flow approximation with success. In many sources(Shames, 1992, Incropera and Dewitt, 1993), it is reported that if the aspect ratio (width/height) of a channel is larger than 30 then Poiseuille flow is an excellent approximation. Care will be taken to check the value of the aspect ratio of the channels used in these experiments.

1.5 RESEARCH OBJECTIVES

There are two primary objectives in this thesis. The first is to experimentally determine the necessary flow conditions to detach an adhered air bubble from a slit microchannel. The second is to find a theoretical model that satisfactorily predicts the necessary flow conditions.

1) The first goal of this thesis to accurately quantify the flow requirements to remove an attached bubble of air inside extremely small channels. The flow requirements will be found in terms of critical flow velocity, channel height, h, and bubble contact diameter, D_c. The critical flow velocity will be found by creating different combinations of D_c and h and experimentally determining the required flow velocity to detach the bubbles from the surface. Each experiment will begin by creating a combination of D_c and h and then proceeding to increase the flow rate until the bubble is dislodged from its initial position. This will be repeated for a wide range of D_c and h. The results will be presented in terms of the Capillary

number corresponding to the critical flow velocity and the ratio D_c/h. The experiment procedure is documented in full in Chapter 2.

2) The second goal of this thesis is to develop a model that can predict the data found in the experimental stage. A model will be derived by formulating approximations for both the drag force acting on the bubble to dislodge it and the surface adhesion forces acting to counter this motion. Equating the two forces will mean the drag and adhesive forces are balanced and the bubble is on the verge of motion. The model predictions will be compared to the experimental results to verify the model's accuracy.

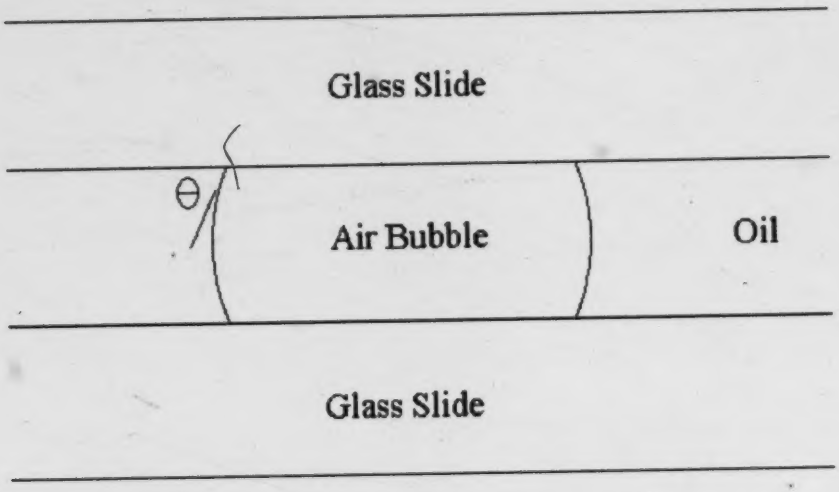

Figure 1.1 - Side view of a bubble inside a slit microchannel

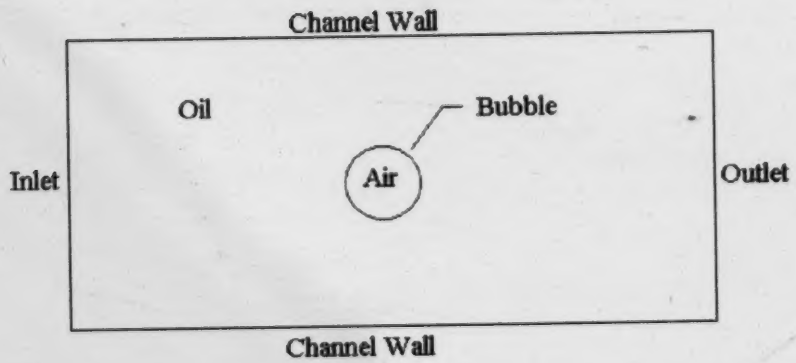

Figure 1.2 – Top view of a bubble inside a slit microchannel

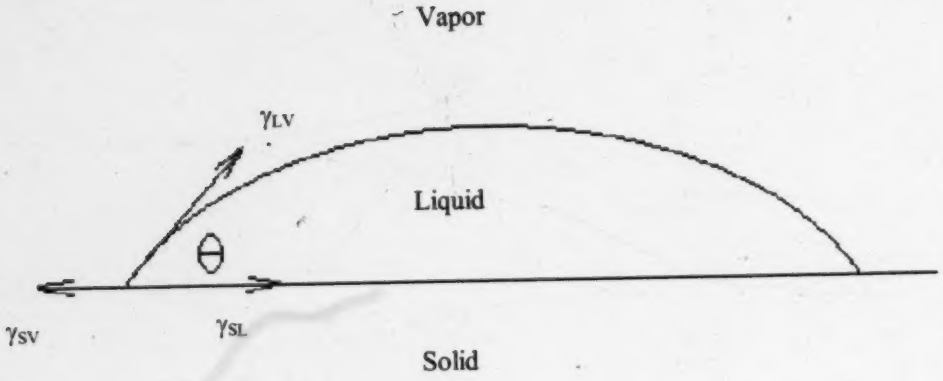

Figure 1.3 - Sessile drop at equilibrium

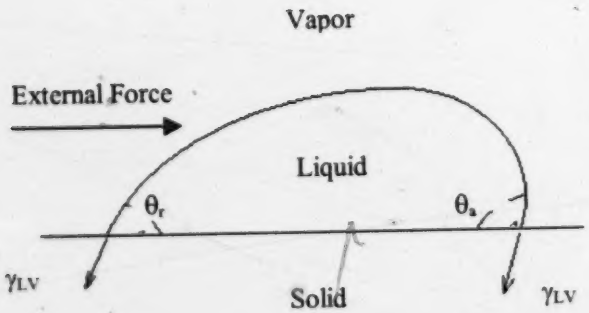

Figure 1.4 - Sessile drop moving along a solid surface

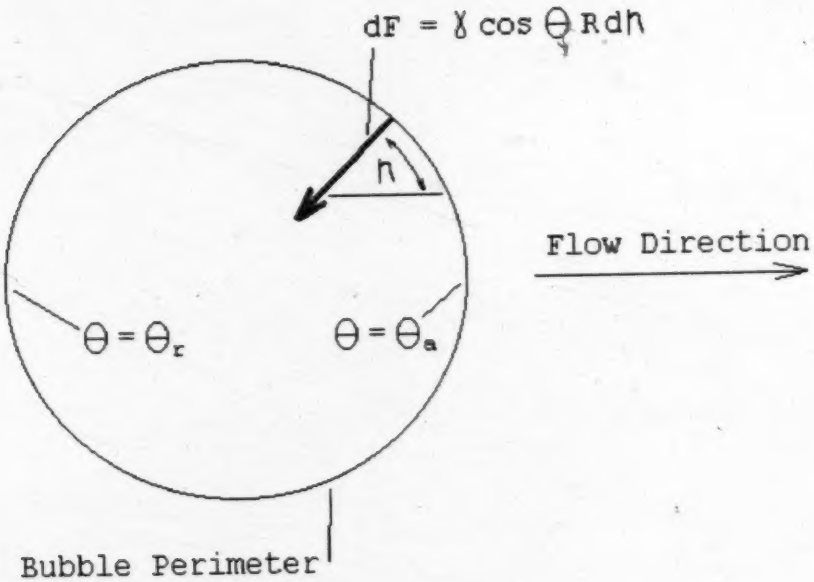

Figure 1.5 - Adhesion force integration setup

CHAPTER 2

CRITICAL STATE DETERMINATION EXPERIMENTS

2.1 APPARATUS

2.1.1 Experimental Overview

To investigate the flow requirements to remove an adhered bubble inside a slit microchannel, several channels were constructed from glass slides and thin strips of plastic shim. The channels ranged in height from 34 μm to 213 μm. Bubbles were created inside the microchannels by injecting air bubbles upstream and manipulating them with buoyancy forces into the center of the microchannel. After bubble adhesion was confirmed the bubbles were removed by gradually incrementing the flow rate and allowing the system to reach steady state. The steady state at which the bubble begins to slide was deemed the critical state and the mass flow rate and pressure drop were recorded. The following sections will describe the apparatus and technique necessary to conduct this experimentation.

The apparatus was comprised of a single stroke precision pump manufactured by Ruska, a plexiglass test cell, a Validyne digital pressure transducer and display, a CCD digital camera and Leica microscope connected with a SUN computer imaging system, and assorted globe valves and tubing. The apparatus was arranged as shown in the block diagram in Figure 2.1. The apparatus will be described in more detail in the following sections.

2.1.2 Computer Imaging System

The computer imaging system is simply depicted as part of Figure 2.1. A Cohu 4910 CCD monochrome camera is mounted upon a Leica Wild M3B microscope. The video signal generated is transmitted first to a Sanyo black and white video monitor and then to a VideoPix digital video processor. The video processor was used to record the signal and digitize the image to a resolution of 640 x 480 pixels with 256 gray levels where 0 represents white and 255 represents black. A Sun Sparc 10 Unix computer was used to operate the digital video processor and to analyze the data. The software package which includes the axisymmetric drop shape analysis-profile technique (ADSA-P) (Cheng et al., 1990), was utilized to digitize the images recorded and to select points of interest. The ADSA-P algorithms will not be used in this portion of the experiment but will be used in later sections dealing with contact angle measurement.

Before the experiments could begin, the magnification of the microscope had to be determined. A grid containing calibrated squares of length 250 μm was imaged and digitized for each microscope magnification setting. By comparing the physical dimensions of the square to the dimensions of the squares in pixels it is straightforward to find the calibration factor. Three different magnification factors were used in this study. The calibration factors determined for each magnification are given in Table 2.1. The 25X and 40X settings were the most frequently used settings. The 16X setting was used only once and 6.4X was used primarily to align the bubble in the microscope's field of vision before zooming in and focusing.

During the experiments the camera was always oriented as to be looking straight

down at the bubble inside the microchannel. It is important that the camera be perfectly vertical as to image the contact diameter correctly. Viewing the bubble contact diameter at even a small angle from vertical would distort the image and ultimately give erroneous values for the bubble contact diameter.

In this experiment it was necessary only to select points along the perimeter of the bubble contact zone using the digitized images. The x-y coordinates in pixels were written to an output file. This series of digitized points about the bubble contact perimeter could then be analyzed to determine the bubble contact diameter.

The coordinates were used to perform a sum of squares minimization curve fitting algorithm to the selected points. The perimeter of the bubble was fit with a circular profile. The algorithm's output was the center of the circle and the bubble contact diameter in pixels. A custom Fortran code was developed to accomplish this task and is available as Code 2.1 in Appendix A. The diameter could be converted from pixels to micrometers using the calibration scale of the microscope at the proper magnification.

The imaging system was also used to determine the channel height prior to insertion into the test cell. By digitizing the images of the cross-section of the channel, points of interest are selected from which the channel height can be found. However, the insertion of the channels into the test cell caused these values to change and thus cannot be trusted. This will be discussed further in the next section.

2.1.3 Microchannels

A typical microchannel assembly drawing is shown in Figure 2.2. The slit

microchannels are constructed with 2 glass slides (15 mm x 30 mm x 1 mm) separated by 2 strips of plastic shim (15 mm x 2 mm) of various thickness acting as spacers. The two plastic shim strips are placed lengthwise along the periphery of the glass slides and then glued into place using Devcon 5 minute epoxy. Before construction, the glass slides were prepared with 3M FC-725 fluorocarbon coating to ensure that surfaces would be very smooth and hydrophobic. The coating procedure is documented in Section 2.2.1. The hydrophobic characteristic was desired to expedite bubble adhesion and to increase the bubble's equilibrium contact angle. This will provide a stronger resistance to detachment and thus allow a large range of flow rates to be tested before the bubbles are removed. Preliminary testing showed that the bubbles were detached with extremely small flow rates and this was the motivation behind coating the surfaces. The completed slit microchannel was then glued into the slots inside the plexiglass test cell with Deveon 5 minute epoxy and allowed to set. Completed channels ranged in height from 34 - 213 μm with a width of 11 mm.

For each channel constructed, it was necessary to determine the channel height. The channel heights were measured prior to insertion into the test cell via the computer imaging system, but these measurements were deemed inaccurate because of possible channel expansion or contraction during construction. The height could change due to unaccounted amounts of epoxy infiltrating the cracks between the channel surfaces and the plastic shim. That the two glass plates were kept perfectly parallel after insertion into the test cell could not be verified. It was decided that a set of experiments for each channel would be conducted to determine the correct channel height. For Poiseuille flow through a slit channel, the flow rate is related to the pressure drop and channel dimensions by:

$$\frac{dP}{dx} = \frac{12Q\mu}{Wh^3} \tag{2.1}$$

Hence, to determine the accurate channel height, one could measure the flow rate, pressure drop, and since the fluid properties are known, the height of the channel can be calculated by using Equation 2.1.

In this study, for each channel, the pump speed and bypass valves were adjusted to produce a wide range of flow rates. The pressure drop and mass flow rate were measured at each flow rate setting and used to calculate the channel height. The final result was the average channel height computed for all flow rates. The results in Table 2.2 show a small standard deviation.

2.1.4 Test Cell

A three piece plexiglass test cell was constructed to hold glass slit microchannels of varying height. A diagram of a test cell without a microchannel inserted is given as Figure 2.3. Two narrow slots facing each other in the center of the cell hold the glass slit microchannels in place. The microchannels were orientated with one channel surface glued to the upper surface of the slot. The microchannels used were of various heights, so the unfilled portion of the test cell slot was filled with Devcon 5 minute epoxy to prevent leaking. There are two openings on the upper surfaces of the test cell just upstream and downstream of the microchannel section which were used to connect the pressure transducer taps. There are two additional openings that are used to the connect the cell to the rest of the piping system. The long narrow plexiglass piece is screwed to the other two as shown. This piece

forced all the channels to be of the same length and took much of the loading caused by maneuvering the test cell during the experiments.

2.1.5 Precision Pump

The pump used throughout the study was a Ruska 2248WII proportioning model which operates by advancing a piston forward or backwards through a filled piston chamber at a user specified rate. The speed at which the piston advances is controlled via a gearbox which has 28 different speed settings. However, in this experiment, the primary method of controlling the flow rate was via Valves 1 and 2 (Figure 2.1). By adjusting the degree of openness of these two valves the flow rate could be diverted from the main line to the bypass line, thus altering the flow through the microchannel. The pump's capacity, minimum flow rate, and maximum flow rate are 500 cm^3, 2.5 cm^3/hr, and 560 cm^3/hr respectively. The gearbox could be disengaged and the pump could be operated manually. The piston could then be advanced or retracted by turning a wheel mounted directly to the piston screw. The pump was operated in manual mode for the bubble positioning process and operated with the gearbox for the experiments.

2.1.6 Pressure Transducer

The pressure drop across the slit microchannel was determined using a Validyne Model CD15 pressure transducer. This transducer operated on a diaphragm deflection principle. The degree of deflection of the diaphragm is converted into a voltage which is displayed. The accuracy of the transducer is 0.5% of the full scale reading. The diaphragm,

and hence the full scale reading, was different for each microchannel used and varied from 1-20 psi.

2.1.7 Liquid and Air Properties

The testing fluid was a base engine oil (MCT-30 - Imperial Oil) for all 5 microchannels tested. For one microchannel height three different variations of this oil was tested (0%, 1%, and 5% ECA5205 by mass; ECA5205 is a typical polymer additive used in engine oils) to investigate the effects of adding a surfactant. The air bubbles were always formed from atmospheric air at room temperature. The average room temperature was roughly 22°C and did not vary more than 2°C throughout the experiments. Relevant fluid and interface properties at this temperature are given in Table 2.3.

The dynamic and equilibrium contact angles are not listed here as they are the subject of experiments described in Chapter 3.

2.1.8 Miscellaneous Equipment

The bubbles were introduced via a 30 μm syringe fitted into the soft flexible tubing immediately upstream of the test cell. This is depicted in Figure 2.1 as well. Once the air pocket was well inside the system the syringe was removed and replaced with a sewing needle. This was done quickly to ensure there would be no additional bubbles leaking from the syringe tip as the experiment progressed.

The remainder of the piping system consisted of Swaglok aluminum pipe and Swaglok compression copper fittings. All valves in the experiment were Swaglok gate valves. The

valves functioned by turning a knob which blocked the flow in proportion to the amount the knob was turned.

The mass flow rates were found using a Mettler BB240 microelectronic balance and a hand held stopwatch. The balance had a resolution of ± 0.0005 g and the stopwatch had a resolution of 1/100 of a second.

2.2 EXPERIMENTAL PROCEDURE

The following sections describe precisely the experimental technique followed to conduct the experiments. The first section however, describes how the glass slides were prepared prior to the microchannels being constructed.

2.2.1 Coating Apparatus and Procedure

The objective of this procedure was to ensure that a smooth and even coating of FC-725 was applied to one side of a 15 mm x 30 mm glass slide. Prior to the coating procedure, the glass slide should be bathed in acetone and dried several times to ensure a contaminant free pre-coating surface. The glass slide is then taped with a 30 cm long strip of Scotch tape to a stationary stand. Of course, the side of the slide attached to the tape will not be coated well and should be the exterior side of the eventual microchannel. The coating was performed with the apparatus shown in Figure 2.4. Figure 2.4 shows a buoyant platform upon which a beaker of FC-725 coating rests. The platform is floating upon the water's surface. By draining the water away, the platform can be lowered in a very smooth manner. The slide is

then submerged into the coating and the water draining process begins. The draining should be such that the water level will fall at a rate between 0.33 cm/min and 0.5 cm/min. These rates correspond to the coating process taking between 6 and 9 minutes. These values were empirically determined to produce adequately coated slides. The fall of the water level depends upon the water's surface area, draining tube diameter, and the elevation difference between the water's free surface and draining tube outlet, so some practice was required to achieve the desired water level velocity. The resulting coating should appear to be perfectly uniform in thickness and homogenous. The coating will typically take 1-2 hours to become dry enough to handle without danger of marring the surface.

2.2.2 Bubble Positioning and Adhesion

The bubbles were deposited into the flexible tubing upstream of the slit microchannel via a 30 μm syringe. Controlling the flow with the manual piston advance and with the assistance of buoyancy forces, the bubble was positioned near the center of the microchannel. This is a difficult and delicate process that requires some practice. First, by simply tilting the test cell, the bubble will rise to the entrance of the microchannel. At this point, buoyancy forces are no longer sufficient to force the bubble inside the channel. The bubbles formed at the syringe tip were always much larger than the height of the channel and would not simply flow inside the channel. Using the manual piston advance it was possible to generate large enough pressures to force the bubble to deform such that it would enter the channel. As a consequence of these large pressures, the flow rate, and thus the speed of the bubble, entering the channel was quite large. When the bubble initially enters the channel it will be carried

along with the flow(i.e., the bubble does not immediately attach to the channel surfaces) quite quickly towards the outlet. The piston must then be immediately retracted to create a negative pressure and halt the bubble before it exits the channel. This requires much practice as retracting the piston too quickly will cause the bubble to speed back towards the inlet. When done properly, the bubble can be stopped approximately in the center of the microchannel. All valves were then fully closed so that the bubble would be undisturbed by flow and adhesion to the upper and lower surfaces of the microchannel could take place. The oil film separating the air bubble from the solid surface slowly thinned, taking on average 30 minutes to reach a stable state. The bubble adhesion process is documented pictorially in Figure 2.5. The images show the process of a typical bubble adhesion process. Figure 2.5a shows a bubble that has just been positioned in the microchannel. The circular line is the oil-air interface. The thickness of the perimeter line is a measure of how much curvature is present in the curvature. This perimeter thickness allows indirect observations of the contact angles to made. This will be discussed in detail in Section 2.3.3.1. Inside the circle is the bulk air phase and outside is the bulk oil phase. At this point, the oil film separating the bubble from the solid surface is completely intact. As time passes, the oil film will thin and drain away. Figure 2.5b is the same bubble 5 minutes later. Visible now are small accumulations of oil inside the bubble. This means that the oil film is both draining away from the bubble to the bulk phase and forming small droplets inside the bubble perimeter. After 25 minutes the same bubble is shown in Figure 2.5c. Now the oil film has reached a steady state. Several oil droplets have formed inside the bubble after having been left behind in the film thinning process. Most bubbles in the experiments took similar lengths of time before

reaching a steady state. It should be noted that although the oil film seems to be completely dissipated from most of the contact surface, this is not the case. A thin film of oil is always present meaning that the surface is always prewetted with oil. This is an important distinction to make when determining the correct contact angles to use. This will be discussed in Chapter 3 as well.

2.2.3 Flow Increment Procedure

The experimental procedure used to increase the flow rate incrementally until the bubble detaches is described below. In the experiment, the system is filled with MCT-30 oil. A bubble of air is introduced in the tubing upstream of the channel using the micro-syringe and is transferred to the center of the channel using buoyancy forces (i.e., tilting the test cell) and by pumping the fluid manually. Thirty minutes was allowed for the bubble to adhere to the surface as described in the previous section. The computer imaging system was used to determine the initial contact diameter of the bubble. The system consisting of the pump and valves was then set to run with a very small flow rate. This initial small flow rate is equal to the flow rate increment which varied from channel to channel. For each channel, it was attempted to keep the flow rate increment as consistent as possible. The primary method of controlling the flow rate increment was by observation of the pressure transducer display. A small but convenient value of a pressure drop increment was chosen. Typically the pressure increment was 0.01 psi for the 213, 164, 122 μm channels and 0.1 psi for the 60 and 34 μm channels. Using Equation 2.1, the approximate corresponding flow rate increments can be solved for. The flow rate increment via Equation 2.1 are approximate rather than exact

because the insertion of an obstructing bubble is sure to alter the pressure drop to some extent. The approximate flow rate increments for each channel are summarized in Table 2.4. The flow increment was difficult to repeat with consistency. The amount of flow that was diverted to the bypass line was extremely sensitive to any change in the gate valve's position. Using extreme caution to rotate the knobs of the valves as small amount as possible was sufficient in most cases to cause the flow to increase by approximately the desired amount. This difficulty in generating small increments will later be shown to be the largest error in the experiment. When the pressure drop reading reached a constant value after approximately 10 minutes, the system had reached a steady state. The system was kept at steady state for 30 minutes while the oil flowed into a beaker at the outlet of the tubing system. The weight of the oil collected was measured using a Mettler BB240 electronic micro-balance. In this manner, the mass flow rate of the oil flow was accurately determined. The steady state pressure drop was also recorded. Using the pressure transducer reading as a guide, the flow rate was increased according to Table 2.4. At the new steady state the flow rate and pressure drop measurements were repeated. This procedure was repeated until the bubble was observed moving with the flow. During the experiment, the bubble's position and contact diameter were observed and recorded by the computer imaging system and the bubble motion can thus be detected. The flow rate and pressure drop at the steady state in which the first bubble motion is detected are considered the critical flow rate and the critical pressure drop.

As mentioned in the above procedure, a period of ten minutes was required for the system to reach a steady state. After this period had elapsed, the position of a line tangent to the upstream side of the bubble was recorded. A period of 2 minutes was allowed to elapse, upon

which the position of the same line was again recorded. If the position of the line had changed appreciably, then motion was deemed to have occurred. To ensure this, the process was repeated for another 2 minute interval. If bubble motion had again been detected, then the flow rate and pressure drop across the channel were recorded as the critical values. Technically, bubble motion does not constitute bubble detachment as the still attached pocket of air is simply sliding along the surface. However, the terms bubble motion and bubble detachment will be synonymous throughout this work.

2.3 RESULTS AND DISCUSSION

2.3.1 Summary of the Experiments Conducted

The independent variables in this study were the channel height, h, and the bubble contact diameter, D_c. The channel width, W, channel length, L, were kept constant at values of 11 mm and 30 mm respectively throughout the experiments. The surface coating (FC-725), fluid density and viscosity were kept constant throughout the majority of the experiments. The fluid density and viscosity were changed slightly by adding a polymer additive to observe any possible effects in the later stages of the experiment. Those results will be discussed separately.

For each channel height used, eight bubbles of different contact diameters were tested. Typically, the bubbles generated fell in the range $2 < D_c/h < 18$ for each channel. Generating large bubbles in small channels proved very difficult as large bubbles were found to have a tendency to shear apart in the positioning process. Thus, the range of ratio D_c/h was kept as

a constant though the range of the contact diameters tested for each channel height was quite different. Following the procedure outlined above, the critical flow parameters causing bubble detachment were determined and recorded. It was found most convenient to represent the critical flow parameters in terms of the critical capillary number:

$$Ca_{cr} = \frac{\mu U_m}{\gamma} \tag{2.2}$$

Normalizing the bubble contact diameter with respect to the channel height results in the dimensionless contact diameter, D_c/h. The critical Capillary number and the ratio D_c/h will be the primary means of presenting and discussing the experimental results.

2.3.2 Two Phase flow Considerations and Bubble Shrinkage

During the course of the experiments, it was noticed that the air bubble's contact diameter would decrease as the experiment progressed. The most likely explanation is that the air molecules would diffuse through the interface into the oil bulk phase. This observation shows that the experiment is actually a two phase flow with the oil phase capable of dissolving the air phase. This phenomenon brought about the need to record the bubble's contact diameter at every flow increment along with the flow rate and pressure. In this section, the molecular diffusion effect will be quantified and its effect on the experiment results examined.

The contact diameter was tracked for all bubbles used in the experiment with the exception of the data at h =213 μm. Of course, this means that the measured values for this channel are inaccurate. This data will not be used for analysis but will be retained for

qualitative comparisons.

Figure 2.6 is plot of the behavior of the bubble contact diameter during the experiments with h=164 μm. Each curve represents the data for one bubble test. In each case, the contact diameter decreases monotonically as the pressure drop across the channel increases. There seems to be no identifiable pattern as to how the contact diameter decreases. There also seems to be no rule as to how much the contact diameter will decrease by. Several bubbles shrank extensively while the contact diameter decrease was small for others. Clearly, this is a complex phenomenon which is difficult to explain.

The molecular diffusion did not only occur when there was a flow present. Two bubbles were placed inside the h=164 μm channel and left there for a period of nearly three days. Images of the bubbles were taken at regular intervals and the contact diameter computed. Figure 2.7 is a plot of the results obtained. Both bubbles became smaller as time passed. The smaller bubble completely dissipated at roughly t=1.5 days. The larger bubble eventually reached a steady value. Possibly, the oil had reached its air saturation limit at this point. Comparing Figure 2.6 and Figure 2.7 shows the rate of bubble shrinkage is much faster when a shearing flow is present.

The decreasing of the contact diameter is clearly not a minor effect and how this may effect the data must be analyzed. The shrinking did not affect the measurement of the critical state. The rate at which the bubble's contact diameter decreased was not large enough for it to be mistaken for motion. When the bubbles began to slide, the velocity was large enough to be seen clearly. The shrinking of the bubble was a gradual process which was not detectable by simply observing the bubble. By recording the bubble contact diameter during

the course of the experiments, the accuracy of the data was not comprised by the gradual shrinking of the bubble.

2.3.3 Critical State Results

2.3.3.1 Contact Angle Hysteresis

As discussed in Chapter 1, with an attached bubble subjected to some external force, the contact angles will change to resist motion. In this experiment, the bubbles are subjected to drag forces and a change in the contact angles was expected. From the vantage point of looking straight down at the bubble, the curvature of the interface should be seen to change with a change in the contact angles. Figure 2.8 demonstrates this more clearly. The angle, θ, is the contact angle. It is customary to measure the contact angle on the liquid side. However, it was more convenient in this study to measure the contact angle from the air side and this was done in the remainder of this work. The oil-air interface casts a shadow which is visible as a dark line about the bubble perimeter. The thickness of the interface shadow is indicative of the value of the contact angle. If, in Figure 2.8, $\theta = 90°$, then the interface shadow would be very narrow. If θ was closer to 180°, then the interface shadow would be much thicker. The changing of the contact angles were observed during the experiment by examining the camera images. A sequence of images taken during the course of one experiment are presented as Figure 2.9. It is expected that the contact angles on the downstream side should be larger than θ_e, and the contact angles on the upstream side should be smaller than θ_e. Thus, the increased contact angle on the downstream side should cause the oil-air interface to deflect a greater distance outwards away from the bubble center. This

will cause a thick interface shadow. The upstream interface should behave in the opposite manner and shift towards the bubble center. This will cause a thin interface shadow. Both phenomenon can be seen in Figure 2.9. Taking note of the direction of the flow (the arrow points in the proper direction), one can observe that the darkened line which represents the oil-air interface shadow becomes thicker on the downstream side and thinner on the upstream side.

2.3.3.2 Critical States

The experimental results for all tested channel heights are shown in Figure 2.10. The presents the data in terms of Ca_{cr} multiplied by 1000 versus D_c/h. The best fit line to this data is $1000Ca_{cr} = -0.0036(D_c/h) + 0.426$ which is a linear relationship. The data for h=34 μm shows that Ca_{cr} has little dependence upon D_c/h as the slope of the curve(-0.0036) is very near zero.

The experimental results for the channel height of 60 μm are also shown in Figure 2.10. Again it is seen that Ca_{cr} has little dependence upon D_c/h. The equation for the best fit line is $1000Ca_{cr} = -0.0024(D_c/h) +1.00$. In comparison to the data for h=34 μm, the critical Capillary numbers for h=60 μm are greater than those found for the smaller channel. The relationship again seems to be linear as the best fit line agrees well with the data.

The data from the experiments with h=122 μm are given in Figure 2.10 as well. At this channel height, the critical Capillary can be seen to be a function of D_c/h. The critical Capillary number is seen to decrease as the bubble contact diameter increases. In general, Ca_{cr} at this value of h, is larger than the values found for the smaller channels. Once again the

relationship seems linear as indicated by the agreement of the linear regression line. The equation of the best fit line is $1000Ca_{cr} = -0.1081(D_c/h) + 2.895$.

The critical values obtained for the experiments with h=164 μm are given in Figure 2.10. The dependence of Ca_{cr} upon D_c/h is apparently linear as shown by the linear regression curve. The critical Capillary number decreases as the contact diameter increases. The equation of the best fit line is $1000Ca_{cr} = -0.1576(D_c/h) + 4.128$. Comparing the data with the data from the other channel heights shows that in general, Ca_{cr} is larger for this channel height.

The relationship seems to be linear for each set of data. For each value of h, Ca_{cr} decreases as D_c/h increases. In simpler terms, the smaller bubbles require a stronger shear flow than the larger bubbles to be removed. Intuitively this trend makes sense, as one would expect that the drag force on a tiny bubble should be much smaller than on a large bubble. Another trend visible from Figure 2.10 is that the largest Ca_{cr} were found for the largest channel sizes. This means that for similar geometrical situations, the bubble existing in the larger channel would be more difficult to remove. Another interesting trend is the decreasing dependence of Ca_{cr} upon D_c/h as the channel height decreases. As h decreases from 164 μm to 34 μm the slope of the curves decreases from –0.1576 to essentially zero.

2.3.3.3 Other Fluids and Repeatability

To investigate whether the same trends would be observed with a oil of slightly different composition two different oils were created by adding 1% and 5% by mass quantities of the surfactant ECA5205 (Imperial Oil) to the base oil MCT-30 (Imperial Oil). The effect

of the surfactant was to slightly alter the oil viscosity and density(<1%) and to change the surface tension a small amount as well. ECA5205 is a popular additive in the oil industry so it is desirable to observe any changes in the experimental results from its use. The entire piping system was flushed repeatedly with the altered oil to ensure that the composition of the oil would not be in doubt before proceeding. The experimental data did not show any appreciable change from the unaltered oil tests. This combined with the very small changes in the oil's viscosity and density made these experiments a repeatability test. The new fluids were tested at only one channel height (122 μm). Figure 2.11 shows the results in comparison to the data recorded with the unaltered base oil. The data points all gather about the original data without significant deviation, which confirms the repeatability of the measurement process.

2.3.3.4 Explanation for Experimental Scatter

Some of the deviation of the data points from the best fit curves can be explained by examining the shapes of the bubbles. Most of the bubbles were close to circular as was expected, but there were exceptions. Some of the bubbles did deform during the experiments as they lost volume. The reason could be uneven molecular diffusion through different sections of the interface or an imperfect coating causing the bubble to prefer certain parts of the surface over others. Of course, having a bubble of non-circular perimeter will dramatically change the value of the drag force and hence where the critical state occurs. Figures 2.12-2.15 catalog the contact perimeters of the bubbles formed during the experiment. The original images were discarded but the x-y coordinates of the selected

perimeter points were saved. The figures were generated by mapping the perimeter points according to the proper microscope scale. The direction of the flow is approximately from the lower left to the upper right in each case as per the arrow in Figure 2.9. The vast majority of the bubbles generated remained near circular at the critical state but there were some notable exceptions. Some bubbles (Figure 2.14d, Figure 2.15g) deformed to an ellipse like shape with the major axis parallel to the direction of the flow. Other bubbles (Figure 2.12f, Figure 2.13f) deformed to shapes that were circular but with odd curvatures spoiling the circular perimeter. That the bubbles were not all perfectly circular at the critical state explains some of the scatter present in the data.

2.4 PHYSICAL EXPLANATION OF OBSERVED TRENDS

First, that Poiseuille flow exists within the microchannels should be verified as many of the following arguments assume this. In Chapter 1, it was shown that if the aspect ratio of the channel is larger than 30, then Poiseuille flow is an excellent approximation. The channels tested in these experiments ranged in height from 34 μm to 164 μm with a constant channel width of 11 mm(11000 μm). The aspect ratios can readily be shown to range from 67 to 324. The conclusion is that assuming Poiseuille flow is valid for all the channels tested.

To explain the trends observed in the data, the behavior of the drag force as the bubble contact diameter and channel height change can be examined. It is reasonable that a bubble with a larger diameter should experience a larger drag force than that experienced by a smaller bubble. The large bubble will simply block more of the channel and will have a

larger surface area upon which pressure and viscous drag forces can act. If the discussion is limited to a specific channel height, this explains why the smaller bubbles require a larger shearing fluid velocity for detachment. Examining the Poiseuille equation, Equation 2.1, reveals that the pressure gradient in the channel is inversely proportional to h^3. It is logical to assume that the pressure drag force then will get large very quickly as the channel height decreases considering the same bubble contact diameter and flow velocity. However, the critical flow velocities were found to be smaller in the smaller channels. This will cause a decrease in the drag force. Equation 2.1 shows that the pressure gradient is proportional to U and so the drag force will correspondingly decrease in the same way. Another factor is that for similar bubble contact diameters, the surface area on which the drag forces can act gets smaller with h. In summary, there are three factors to consider when decreasing the channel height: the critical flow velocity decreases and will lessen the drag force, the surface area decreases linearly with h and should lessen the drag force, and the pressure gradient increases in a cubic manner with decreasing h and this will increase the drag force. From the data, it is obvious that the increase in the pressure gradient dominates the effects of the lower velocities and decreased surface area.

The data shows that for similar bubble contact diameters the larger drag was present on the bubble in the smaller channel. To demonstrate that this indeed is the case, the experimental data is redrawn as U_{cr} versus D_c in Figure 2.16. It is clear from this plot that in a range of similar contact diameters, the bubbles in the smaller channels were easier to remove, i.e., the critical velocity was smaller for smaller channels. The final observable trend is the seemingly lack of dependence of Ca_{cr} upon D_c/h at smaller channel heights. This can

be explained by examining the range of contact diameters tested for h=60 and h=34 μm. The difficulties in generating bubbles with large contact diameters caused the range of D_c for the smaller channel heights to be limited. A dependence upon D_c was not established as the range of D_c was too small. It seems reasonable to think that if larger bubbles were possible in the smallest channels, then the required shearing velocity should be quite small and a variation of Ca_{cr} would be observed. For that reason, the data when presented in terms of D_c/h is somewhat misleading in terms of the trends that can be identified. Plotting in terms of D_c/h exaggerates the range of bubble contact diameters that were actually tested. Physically, it should be impossible for the critical capillary number to have no dependence upon the contact diameter. For example, as D_c approaches the channel width, W, any flow rate greater than zero will cause the bubble to move as the bubble would be completely blocking the span of the channel. If the channel becomes blocked off then the pressure force on the bubble would quickly increase and easily overcome the adhesive force. This would result in $Ca_{cr} \sim 0$. Therefore, all the curves present in Figure 2.10 must cross the D_c/h axis at some point corresponding to $D_c=W$. This point on the axis will be different for each channel height. For h=164 μm the point should be $D_c/h=67$. The data for h=122, 60, and 34 μm should eventually cross the D_c/h axis at $D_c/h=90$, 183, and 324 respectively. Trying to extrapolate the experimental data to confirm this is difficult as the nature of curves is not guaranteed to be linear and the scatter in the data adds uncertainty to any extrapolation performed. However, recognizing that the data must behave in a manner to cross the D_c/h axis at the points outlined above does explain why the curves have different slopes for different values of h. The curve for h=164 μm must decrease faster that its counterparts at smaller channel

heights as it must cross the axis at a smaller value of D_c/h. The curves for h=60 μm and h=34 μm show very small slopes in part because of the narrow range of D_c tested and in part because theoretically they cross the D_c/h axis at very large values of D_c/h.

2.5 UNCERTAINTY ANALYSIS

The accuracy of the experimental data will be discussed in this section. All measured quantities taken will be considered and conclusions regarding the accuracy critical state parameters will be made.

2.5.1 Pressure Measurements

The pressure transducer had an accuracy of 0.5% of the full scale reading. To accommodate the large range of pressure drops the full scale reading had to be adjusted for each channel height. The channels with h=213 μm and h=164 μm required a full scale reading of 1 psi. For h=122 μm, the full scale reading was 2 psi and for both the h=60 μm and h=34 μm the full scale reading was 20 psi. The accuracy for the pressure reading is then ± 0.005 psi for the 213 and 164 μm channels, ± 0.01 psi for the 122 μm channel, and ± 0.1 psi for the 60 μm and 34 μm channels. Examining the experimental pressure drops, it seems that the full scale reading is needlessly large. However, the expected pressure drops anticipated during the experiments were not the deciding factor in choosing a full scale reading. The bubbles could be maneuvered with buoyancy forces only to the entrance of the microchannel. From here only a combination of buoyancy forces and pressure resulting from manually advancing

the piston could coax the bubble inside the channel as described in Section 2.2. The required pressures to force the bubble inside the channel were found to be much larger than those encountered in the experiment. Changing the transducer diaphragm after the bubble was inside the channel would not have been feasible as the reinstallation of the transducer into the piping would introduce unwanted air bubbles into the test cell. All the pressures were calibrated to display a maximum of 10 volts despite the thickness of the transducer diaphragm. The transducer calibration demonstrated linear behavior while both increasing and decreasing the pressure as shown in Figure 2.17. The calibration for all diaphragms was performed using an Omega PCL-601 digital pressure indicator.

2.5.2 Mass Flow Rate Measurements

The mass flow rate of the oil was measured by accumulating a mass of oil into a container over a measured period of time. The mass of the oil accumulated was measured using the electronic balance which has a resolution of ± 0.0005 g. The elapsed time was measured with a stopwatch. The mass flow rates throughout all of the experiments was extremely small. The oil would flow through the test cell and after sufficient fluid had accumulated a drop would fall into the waiting container. The container was moved into position after a drop had fallen. The time was started immediately after the initial drop had fallen. The time was ended as the final drop fell and the container was immediately removed. The total elapsed time depended upon how often the drops fell and ranged from roughly 30 minutes for the larger channels to roughly 90 minutes for the smaller channels. An estimate of the accuracy of the time measured taking human error and reaction time into account

would be ±1 second. Typically, the mass of oil collected was less than 1 gram. For each critical state the mass flow was measured three times and an average taken. The equation for the mass flow rate is:

$$\dot{m} = \frac{(m_2 - m_1)}{t} \tag{2.3}$$

where m_1 and m_2 are the initial and final masses of the container, and t is the elapsed time. Following the method outlined by Beckwith et al(1993) to determine the error propagation, it follows that the uncertainty in the mass flow rate measurements is:

$$u_{\dot{m}} = \left(\left(\frac{\partial \dot{m}}{\partial m_1} u_{m_1}\right)^2 + \left(\frac{\partial \dot{m}}{\partial m_2} u_{m_2}\right)^2 + \left(\frac{\partial \dot{m}}{\partial t} u_t\right)^2\right)^{\frac{1}{2}} \tag{2.4}$$

where u_i are the uncertainties in the respective measurements. Taking the appropriate derivatives and substituting results in:

$$u_{\dot{m}} = \left(\left(\frac{-u_{m_1}}{t}\right)^2 + \left(\frac{u_{m_2}}{t}\right)^2 + \left(\frac{u_t (m_1 - m_2)}{t^2}\right)^2\right)^{\frac{1}{2}} \tag{2.5}$$

Evaluating Equation 2.5 for typical data points for each of the channel heights results in very small mass flow rate uncertainties. For example, the uncertainty in the flow rate measurement for a critical state with h=60 μm was $\pm 7.16 \times 10^{-4}$ g/hr(on average ±1.5%). This accuracy is possible because of the lengthy periods in which the fluid was accumulated.

2.5.3 Mass Flow Rate Increment

Though the individual measurement of the mass flow rates can be considered very accurate it is not representative of the error in the mass flow rate at the critical state. The experiment proceeded by increasing the flow rate in small steps. The limiting factor in

adjusting the flow rates was the sensitivity of the flow rate to small changes in the valve knob position. The flow rate could only be changed with consistency by turning the valve's knob a very small distance and waiting for the system to reach a steady state. As mentioned in Section 2.2.3, the pressure transducer reading was the guide to changing the flow rate a consistent amount with each increment. The pressure transducer resolution and the sensitivity to the gate valve adjustment were the limiting factor in how small a flow increment could be consistently reproduced.

The critical state was defined as the first steady state that produced bubble motion. However, the actual critical state could exist anywhere between the previous steady state and the critical state. Thus, the limiting factor in deciding the accuracy of the critical flow rates is the flow rate increment. The flow rate increments given in Table 2.4, show that the resolution of the critical flow rates (i.e., the flow increment) becomes finer and finer as the channel heights decrease. However, the relative accuracy worsens as the channel heights decrease because the magnitude of the flow rates gets smaller. A typical percentage error (error/reading) for the largest channel height of 164 μm is ±4.1%, while for the smallest channel height of 34 μm the percentage error is typically ±17%. The large errors at the smaller channel heights are clearly undesirable but unavoidable. The apparatus had limited flow rate control and the experiment required the measurement of extremely small flow rates. The critical flow rates for the smallest channel were measured at values around 0.05 g/hr.

2.5.4 Bubble Contact Diameter Measurement

The contact diameter of the bubbles was determined by the computer imaging system and a circular curve fitting algorithm. The perimeter points were manually selected at about 70-80 points about the contact line. It can be assumed that regardless of the camera magnification the selection of the perimeter points could be done with the same degree of accuracy. The points were chosen with great care and only where the contact line was sharp. A reasonable estimate of the precision in the selection is ± 1 pixels in both directions. It is not clear how the uncertainty in the position of so many perimeter points will propagate through the sum of squares minimization algorithm. Assuming that instead of using this algorithm, two perimeter points that would constitute the correct bubble contact diameter are chosen, then the uncertainty in the measurement of the contact diameter can be found in an RMS manner as follows:

$$u_{D_c} = (u_{x_1}^2 + u_{x_2}^2 + u_{y_1}^2 + u_{y_2}^2)^{\frac{1}{2}} \qquad (2.6)$$

where x_1, x_2, y_1, y_2 are representing typical pixel coordinates. This equation evaluates to an uncertainty in the bubble contact diameter of ± 2 pixels. For the most frequently used microscope magnification factor (x25) this corresponds to an uncertainty of ±13 μm. However, there are other forms of error possible in this measurement. The bubbles are not all perfectly circular as the curve fitting algorithm assumes. The effect of this 'shape error' is difficult to quantify other than to explain the scatter in the data as done in Section 2.3.

2.5.5 Channel Height Measurement

The height of the channels was determined by pumping oil through the channels at different flow rates without any bubbles present. The pressure drop across the channel and the mass flow rate were determined and by using Equation 2.1, the channel height could be determined. The calculated channel heights showed a small standard deviation with a maximum value of 2 μm for the largest tested channel.

2.5.6 Error Propagation - Critical Capillary Number

The capillary number is a nondimensional quantity as shown in Equation 2.2. It is dependent upon the oil viscosity and oil/air surface tension. These quantities will be assumed to be exact for this discussion. The average flow velocity is a derived quantity which is computed from the measurements of the volumetric flow rate and the channel height as follows:

$$U_m = \frac{Q}{Wh} \tag{2.7}$$

and the uncertainty in the average velocity is found by:

$$u_{U_m} = \left(\left(\frac{1}{hW} u_Q\right)^2 + \left(\frac{-Q}{h^2 W} u_h\right)^2\right)^{\frac{1}{2}} \tag{2.8}$$

The uncertainty in Q is the uncertainty in the mass flow rate measurement but corrected for the difference in units. To relate the uncertainty in the mean critical velocity to the uncertainty in the critical capillary number, simply multiply by μ/γ(the fluid characteristics are considered to be known exactly). Evaluating Equation 2.8 for a typical data point at

h=164 μm results in an uncertainty in Ca_{cr} of ± 9.67×10^{-5}. The same calculation for a h=34 μm data point results in an uncertainty in Ca_{cr} of ± 7.24×10^{-5}. These absolute uncertainties correspond to relative uncertainties of ± 4.9% and ± 18.0% for the 164 μm and 34 μm channels respectively. This leads to the conclusion that the measured data is more reliable with the larger channels than with the smaller channels.

2.5.7 Error Propagation - D_c/h

In the previous sections it was found that the uncertainty in the bubble contact diameter could be estimated as being ± 13 μm for most measurements and that the largest uncertainty in the channel height was ± 2 μm. Following the same procedure as in the previous section the uncertainty in the ratio D_c/h can be shown as:

$$u_{\frac{D_c}{h}} = \left(\left(\frac{1}{h} u_{D_c} \right)^2 + \left(\frac{-D_c}{h^2} u_h \right)^2 \right)^{\frac{1}{2}} \tag{2.9}$$

Evaluation of Equation 2.9 for both h=164 μm and h=34 μm and D_c/h=10 (i.e., using a fictitious measured diameter to create the ratio 10), uncertainties in the ratio D_c/h of ± 0.14(±1.4%) and ± 0.69(±6.9%) are found respectively. Once again, the largest uncertainties are found with the smallest channel height. Equation 2.9 shows that larger bubble contact diameters will result in larger uncertainties in D_c/h.

2.5.8 Conclusions regarding Experimental Data

The method of presenting the data has been to plot the critical capillary number versus the ratio of D_c/h. It is clear that the data has errors in both these quantities. The data has the

largest relative uncertainties for the smallest channel height of 34 μm. The reason for larger uncertainties for the small channels is that the bubble detaches with an extremely small flow rate. It was difficult to decrease the flow increment sufficiently for this channel to reduce the relative uncertainty due to the limitations of the apparatus.

Overall, and especially for the larger channels, the experimental data has been shown to have small uncertainty in comparison to the quantities being measured. In particular, the results at h=164 and h=122 μm showed a relative uncertainty in the critical capillary number measurements of less than ±12% for most trials. The relative uncertainties became worse as smaller channels were tested due to problems with being unable to generate extremely small flow increments. For all the channels, the measured ratio, D_c/h, had absolute uncertainties of less than 0.7 which is a relative uncertainty of ± 3.5% in comparison to the largest value of D_c/h tested.

Table 2.1 – Microscope Conversion Factors

Microscope Setting	Conversion factor
6.4X	0.03092 pixels/μm
16X	0.0955 pixels/μm
25X	0.1546 pixels/μm
40X	0.2492 pixels/μm

Table 2.2 – Channel Height Measurements

Average Channel Height (μm)	Standard Deviation (μm)
213.4	1.90
163.8	1.03
121.6	0.46
59.8	0.69
33.7	0.33

Table 2.3 – Fluid Properties

MCT-30 at T=22°C	
Density (kg/m^3)	879.2
Viscosity (kg/m/s)	0.286
Atmospheric Air at T=22°C	
Density (kg/m^3)	1.25
Viscosity (kg/m/s)	1.7×10^{-5}
MCT-30/Air Interface	
Surface Tension (N/m)	0.030

Table 2.4 – Approximate Flow Increments

Channel Height (μm)	Approximate Flow Rate Increment (m^3/s)
213	6.57×10^{-11}
164	3.09×10^{-11}
122	3.92×10^{-11}
60	1.54×10^{-11}
34	0.53×10^{-11}

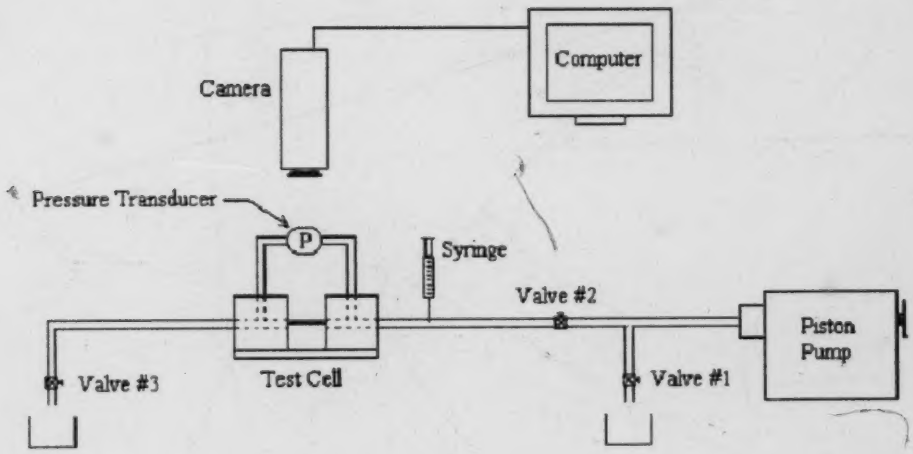

Figure 2.1 – Apparatus Configuration

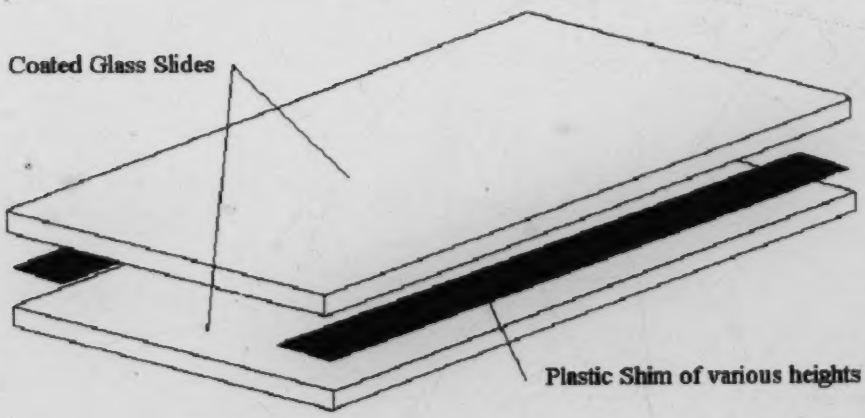

Figure 2.2 – Microchannel Construction

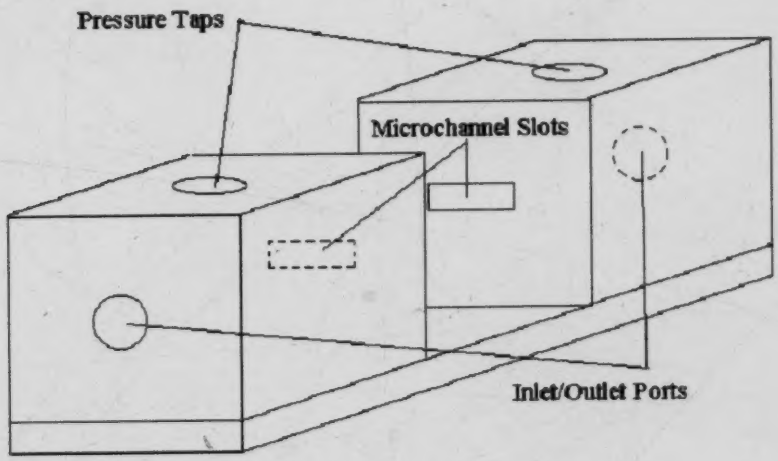

Figure 2.3 – Test Cell Construction

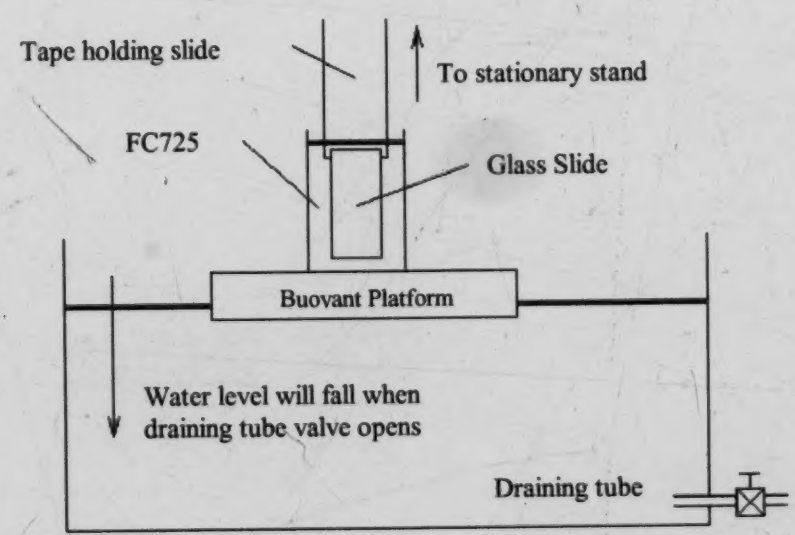

Figure 2.4 – Coating Procedure Apparatus

Figure 2.5a – Bubble adhesion at t=30 seconds

Figure 2.5b – Bubble adhesion at t=5 minutes

Figure 2.5c – Bubble adhesion at t=25 minutes

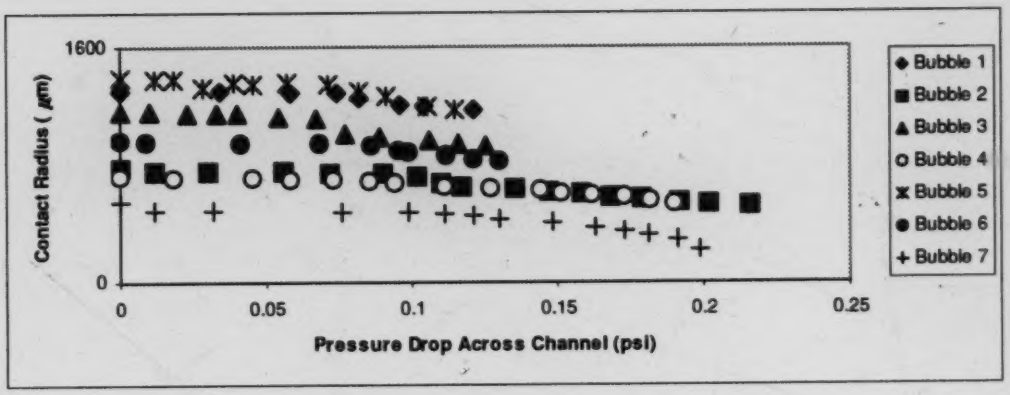

Figure 2.6 – Bubble shrinkage for h=164 μm experiments

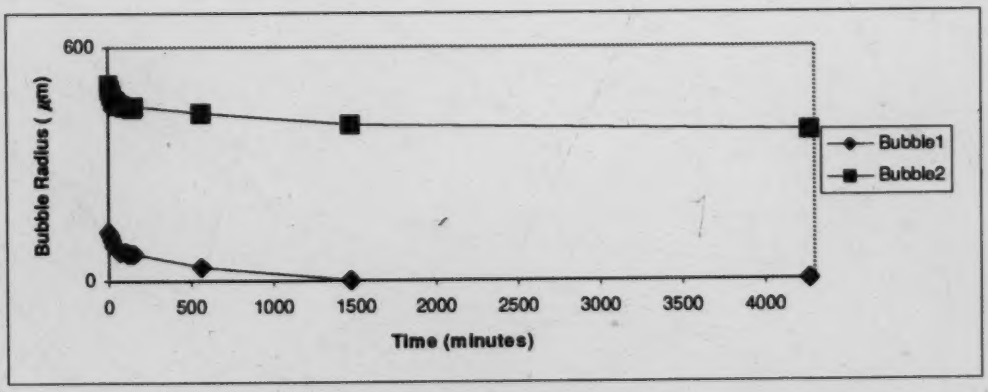

Figure 2.7 – Undisturbed bubble shrinkage (h=164 μm) with time

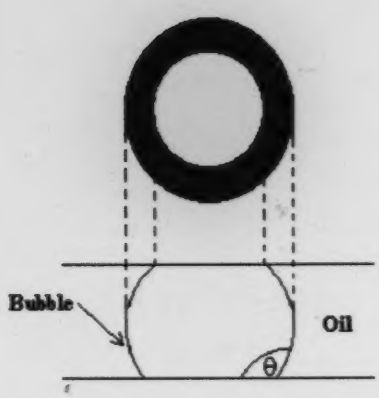

Figure 2.8 – Qualitative relationship of contact angle to interface shadow thickness

Figure 2.9a – Bubble during h=164 μm experiment. The interface shadow thickness is different on the upstream and downstream sides of the bubble.

Figure 2.9b – The same bubble on the verge of motion.

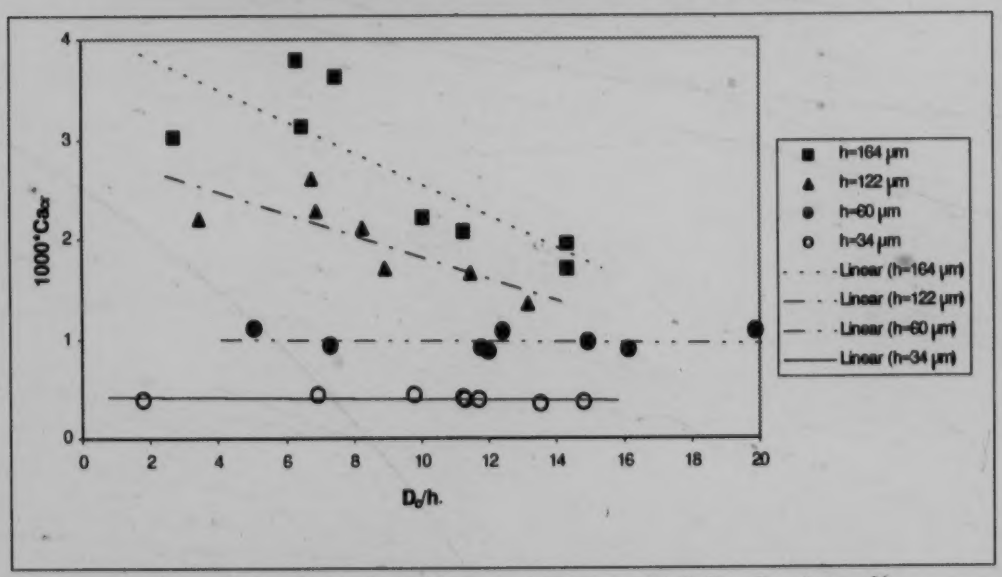

Figure 2.10 – Critical Capillary number versus D_c/h for all values of h.

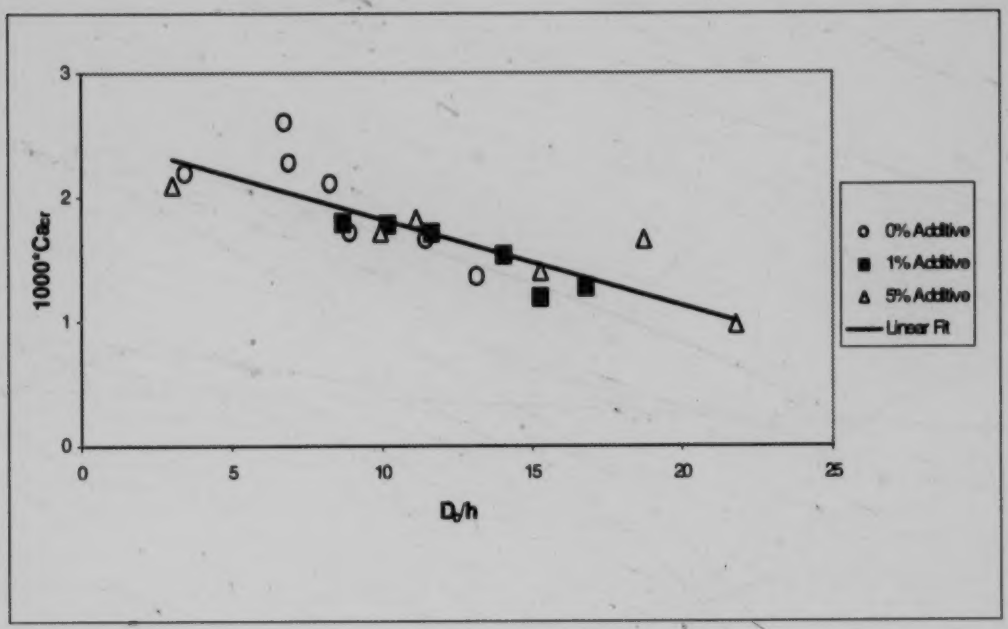

Figure 2.11 – Critical Capillary number versus D_c/h with ECA5205 additive. Channel height is 122 μm for all data points.

Figure 2.12a

Figure 2.12b

Figure 2.12c

Figure 2.12d

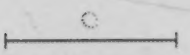

Figure 2.12e

Figure 2.12f

Figure 2.12g

Figure 2.12h

Figure 2.12 – Bubble shapes at critical state for the h=34 μm experiments

Figure 2.13a

Figure 2.13b

Figure 2.13c

Figure 2.13d

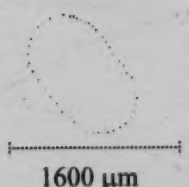

Figure 2.13e

Figure 2.13f

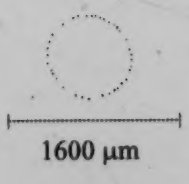

Figure 2.13g

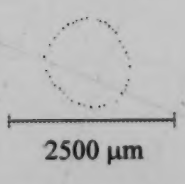

Figure 2.13h

Figure 2.13 – Bubble shapes at critical state for h=60 μm experiments

Figure 2.14a

Figure 2.14b

Figure 2.14c

Figure 2.14d

Figure 2.14e

Figure 2.14f

Figure 2.14g

Figure 2.14 – Bubble shapes at critical state for h=122 μm experiments

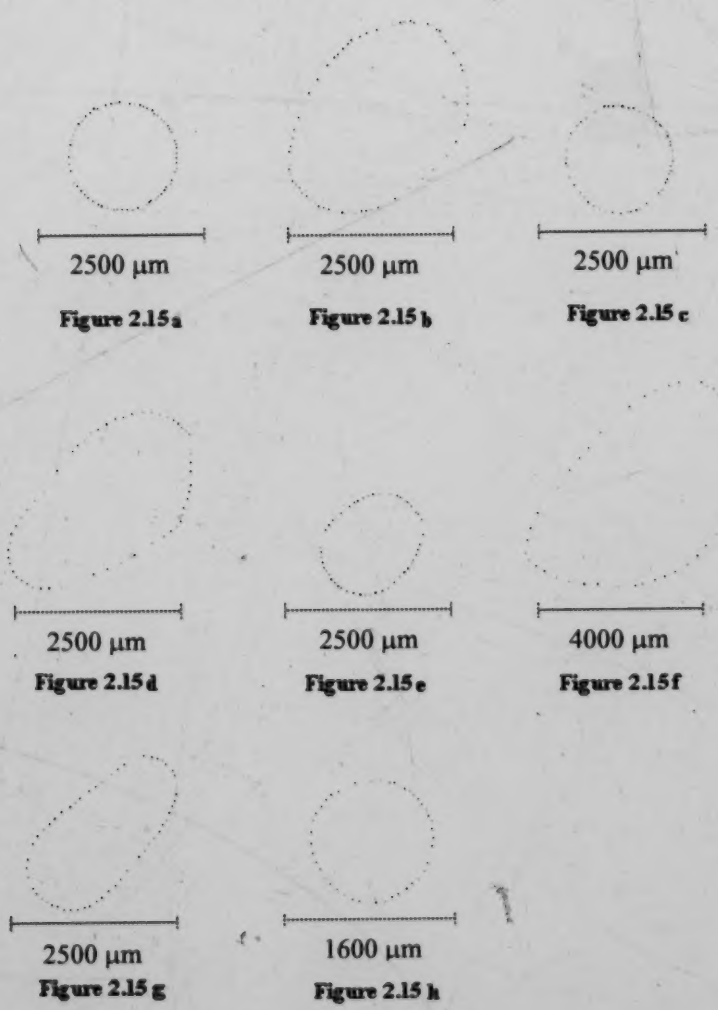

Figure 2.15 – Bubble shapes at critical state for h=164 µm experiments

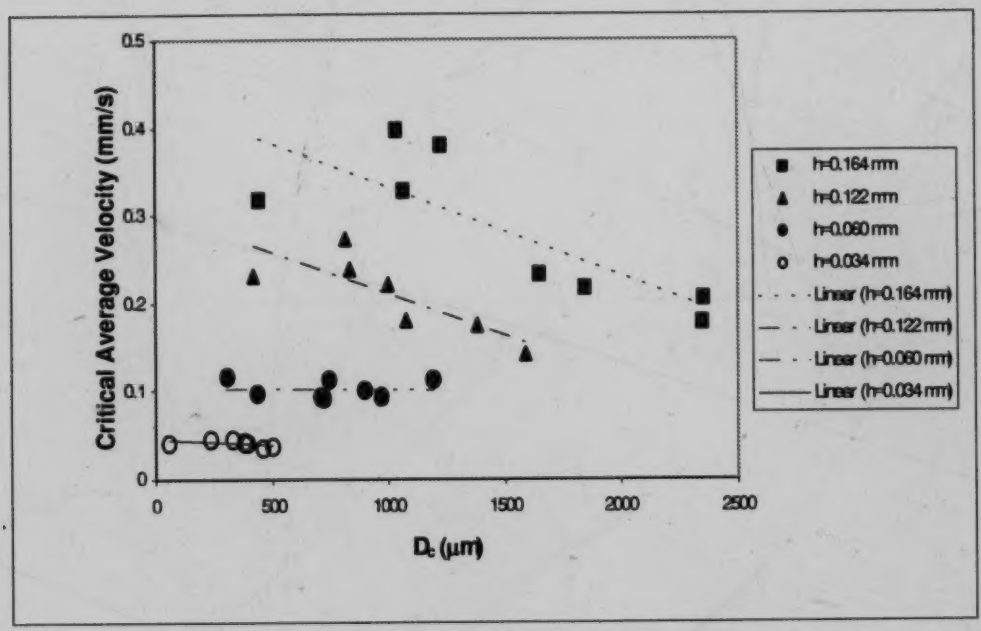

Figure 2.16 – Critical average velocity versus D_c

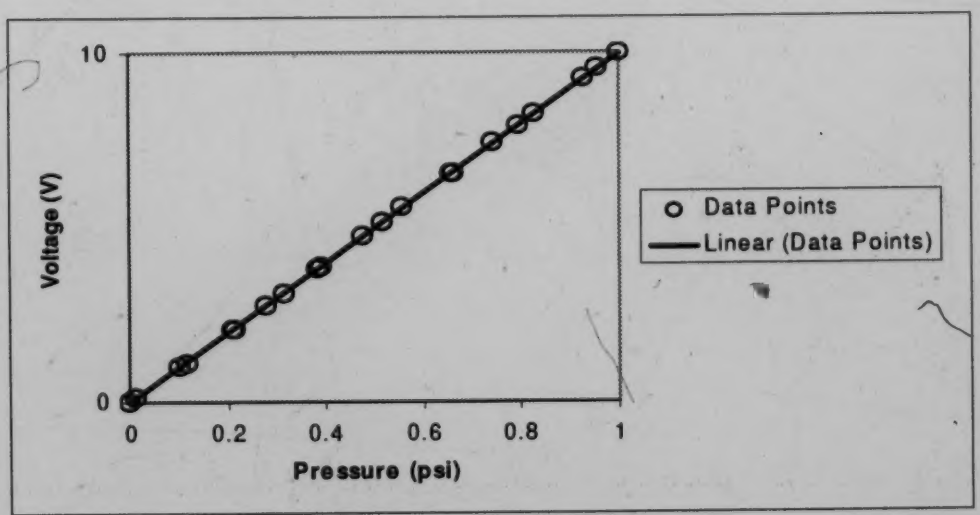

Figure 2.17 – Pressure transducer calibration curve for the 1 psi diaphragm

CHAPTER 3

CONTACT ANGLE MEASUREMENTS

3.1 MOTIVATION

As discussed in Chapter 1, the retaining force of the bubble will be dependent on the value of the advancing and receding dynamic contact angles. In order to evaluate the adhesion force correctly it is necessary to determine the surface tension of the MCT-30 in air along with the advancing and retreating dynamic contact angles. The dynamic contact angles that were present in the experiments of Chapter 2 could not be directly measured as there was no way of viewing the bubbles contact region with sufficient resolution. As discussed briefly in Chapter 1, the dynamic contact angles will depend upon the height of the channel as well as the Capillary number. In this experiment, the maximum static advancing and receding contact angles will be measured. These values will represent the extreme values of the dynamic contact angles. In effect, the range of the possible dynamic contact angles will be determined. The surface tension has been measured to be a value of 0.030 N/m [Gu and Li, 1996] using the ADSA-P software package [Cheng et al, 1990]. It is the goal of this experiment to determine the extreme values of the advancing and receding dynamic, and equilibrium contact angles for an air bubble in MCT-30 attached to a prewetted FC-725 surface. The equilibrium contact angle of a MCT-30 sessile drop on a dry FC-725 surface has been measured [Gu and Li, 1996] as 78.6°. This angle cannot be used however as the surfaces in the experiments of Chapter 2 were prewetted with oil before the air bubbles were

introduced. This difference is important as a thin oil film will always be present between an adhered bubble and the surface for a prewetted surface. The same cannot be said for a dry surface. The presence of an oil film will cause the oil to easily wet the surface and thus change the physics of the situation.

3.2 PROCEDURE AND EQUIPMENT

An experiment similar to the one conducted by Macdougall and Ockrent(1942) was modified to fit the needs of this study. In Macdougall and Ockrent's work, a droplet is deposited onto an inclined surface and allowed to reach an equilibrium position. Gravity produced an external force on the drop and the contact angles deformed to hold the drop in place. In the present work, an investigation similar in nature to this will be performed. Air bubbles will be generated on the underside of a coated plate. The plate will then be inclined and the effect on the contact angle hysteresis will be observed. The angle of inclination will increase until the air bubble is dislodged.

The apparatus for this test in shown in Figure 3.1. A 15 mm x 30 mm x 5 mm aluminum plate(polished with 0.05 μm grit) coated with FC-725 was supported by two plastic supports. The plate and supports are inside a plexiglass container which is filled with MCT-30 engine oil. An aluminum plate was used to facilitate construction. That a metal plate is used rather than a glass slide(as per the construction of the microchannels) is inconsequential as it is the coating that the bubble will be adhered to. The surface chemistry will be identical regardless of the material the plate is made with. A hole of diameter 250 μm is drilled in the

center of the metal and a capillary tube with an outside diameter of 200 μm is inserted and glued into place using Devcon 5 minute epoxy. The inside diameter of the tube was 30 μm. A flexible nylon tubing with an inside diameter of roughly 250 μm was fitted over the capillary and the other end of the tubing was used to connect to a syringe pump again using Devcon 5 minute epoxy to maintain the connection. The syringe pump was controlled with an Anahiem Automation (Model # DPF72) Controller which directed the rotational speed and rotational direction of an Anahiem Automation Miniangle stepper motor (Model # 23PM-C402). The stepper motor had a resolution of 1.8 degrees/step. The motor rotated a screw which in turn advanced the syringe plunger. The screw had 21 threads per inch which translates into a forward displacement of the syringe plunger of 2.38×10^{-4} inches per motor step. The syringe cavity was filled with air. The coated plate was positioned such that the hole would be approximately in the middle of the two plastic supports. The plexiglass container has a glass window on the side orientated towards the digital camera setup to allow for an unobstructed view of the bubbles. Initially the plexiglass container is resting on a flat, horizontal cast iron lever. The material of which the lever is constructed is not important so long as the lever will remain sufficiently rigid under small loads. Immediately below the lever there waits a Cenco lab jack which be the source of the inclination. By raising the jack, the lever will cause the plexiglass container, plastic supports, and coated plate to incline as shown in Figure 3.1. The same camera system as described in Chapter 2 is used in this experiment as well. The camera should be orientated as to be looking slightly upwards at where the bubbles will form. The camera should be focused with adequate resolution on the circular opening on the underside of the coated plate. The camera looks slightly upwards at the

opening as the true contact angles of the bubble can be observed without possible distortion from the edges of the plate. Again, the camera was connected to the Sun computer imaging system as described in Chapter 2. To provide a clear white background for the camera, a bright light source (Jena Instruments Model # 300246) was directed through a sheet of semi-transparent white plastic. This allowed a sharp bubble profile to be captured by the camera.

Bubbles were generated by directing the syringe plunger to advance at a slow rate until a bubble became visible on the underside of the plate. Once a bubble was observed the syringe plunger was halted and the bubble was allowed to reach an equilibrium position. The lever and thus the coated plate were in a horizontal configuration at this time. To be consistent with the microchannel experiments, the oil film was allowed to reach a steady state before applying an external force to the bubble. A waiting period of approximately 30 minutes was allowed before each trial. Bubbles generated typically had a contact diameter of about 2 mm and the procedure became fairly repeatable with regards to producing a similar sized bubble for each trial. Upon the ending of the 30 minute period, an image was taken of the bubble at equilibrium to evaluate the equilibrium contact angle. The process of inclining the plate then began. The Cenco jack was raised slowly until it made contact with the protruding end of the lever. By further raising the jack, the lever would cause the entire system to be inclined. This inclination will cause a small fraction of the buoyancy force to act on the bubble in the direction of the raised axis of the plate. This external force will be met by the contact angle hysteresis and the changed contact angles will be recorded digitally by the camera and computer imaging system. The jack was raised slowly until a small change

in the bubble's position could be observed on the video monitor display. A period of 2 minutes was allowed for the bubble to reach a new equilibrium after which an image of the bubble was taken. The degree of inclination would then be increased and the process repeated until the bubble detaches and begins to slide along the surface. A bubble on the verge of detaching is given in Figure 3.2. The dark, roughly circular shape is the bubble while the surrounding oil shows up as the white background. This figure gives an excellent view of both the advancing and receding contact angles. The slope of the solid surface demonstrates the direction of the buoyancy force. It can be seen that the advancing contact angle is quite large as was expected from inspection of the images from the microchannel experiments. The images from the microchannel experiments also suggested that the receding contact angle should be near 90° and this is also confirmed qualitatively in Figure 3.2.

3.3 DATA ANALYSIS

The ADSA-P software was utilized to analyze the bubble profile at the angle of inclination just prior to detaching to determine the maximum contact angles. Unfortunately, the software has two failings when it came to this particular application. First, it assumes that the contact angles on both edges will be similar and thus it outputs an average contact angle, which was not the goal of these tests. Secondly, difficulties were encountered while trying to analyze the images due to having contact angles which were near 180 degrees. There is a software option which allows for the bubble profile to be outputted in terms of x-y pixels coordinates. A short FORTRAN code was written (Code 3.1, Appendix A) to fit a 2nd order

polynomial to the bubble profile near the contact zone. The code uses simple trigonometry and calculus to compute the two different contact angles taking account of the inclination angle. The algorithm uses the 20 nearest x-y pixel coordinates in the curve fitting procedure. Figure 3.3 is presented to facilitate the understanding of the computation done here. It is a typical sketch of the near surface profile points used and the curve fitted to this points. The angles θ_a and θ_r are the advancing and receding contact angles respectively.

3.4 RESULTS AND DISCUSSION

3.4.1 Advancing and Receding Contact Angles

In total, eight different bubbles were tested. Each bubble was of a similar size and was generated in the method outlined above. The impending motion contact angles were evaluated using the ADSA-P software along with Code 3.1 in Appendix A. The average advancing contact angle was 163.6° and the average receding contact angle was 112.6°. The experiment showed a reasonable degree of repeatability as the standard deviation for the advancing and receding contact angles were 3.76° and 3.33° respectively.

3.4.2 Equilibrium Contact Angle

The values for the equilibrium contact angles were measured from the generated air bubbles before inclining the plate. The ADSA-P software was used to measure these contact angles. The software uses the digitized images of the bubble to fit a cubic spline to the bubble

profile. The interpolated bubble profile is then analyzed by solving the Laplace Equation of Capillarity. The output of interest from this analysis was the contact angle. An image of one of bubbles tested is shown in Figure 3.4. The average equilibrium contact angle was found to be 140.4° with a standard deviation of 1.1°.

This value for the equilibrium contact can be confirmed by an indirect measurement. Recall the image given as Figure 2.5c. The normal procedure in Chapter 2 is to select perimeter points about the contact perimeter and compute a contact diameter from these points. A different, larger, diameter will be computed if points about the outside of the perimeter line(i.e., the side of the interface shadow farthest away from the center of the circle). Before the bubbles were subjected to any shearing flow, points about both sides of the interface shadow were selected. Thus, the contact diameter and a larger diameter could be found. The difference in these diameters can be used to define a distance, δ, as follows:

$$\delta = \frac{1}{2}(D_{large} - D_c) \tag{3.1}$$

If a circular interface profile is assumed, δ can be related to the equilibrium contact angle as shown by the geometry in Figure 3.5. The approximate expression is:

$$\theta_e = \frac{\pi}{2} + 2\tan^{-1}(\frac{\delta}{h/2}) \tag{3.2}$$

Evaluating Equation 3.2 for the data obtained for each bubble of Chapter 2 prior to testing results in an average equilibrium contact angle of 144.4°. This value is quite close to the value found here of 140.4°. Using this method is far from accurate however. First, the assumption that the interface profile is circular is not verified, and second, the computed value

of θ_e had a large standard deviation of 11.7°. This indirect measurement is still useful in that in provides a qualitative verification of the measured θ_e.

3.4.3 Comparison to Detachment Experiment Observations

This method was ideally suited to measure the maximum static contact angles that could be present in the microchannel experiments. In the microchannel experiments, the FC-725 surface was always prewetted with MCT-30 before the air bubbles were introduced. The coated plate was submersed in MCT-30 before the air bubble was generated in the contact angle experiment so that this condition was met. The bubbles formed inside the slit microchannels were allowed time enough to for the MCT-30 film between the bubble and the FC-725 surface to stabilize and a similar procedure was followed in this experiment as well.

The angles found in this experiment do agree with the observations made in Section 2.3.3.1. The thickness of the oil-air interface shadow was discussed in terms of the contact angles that exist on upstream and downstream sides of the bubble. It was demonstrated that because of the wide interface thickness on the downstream side, an advancing air contact angle close to 180° could be expected. A similar argument showed that the receding contact angle should be much closer to 90° than the advancing contact angle. The measured maximum advancing and receding contact angles support this observation. The maximum advancing contact angle of 163.6° is certainly close to 180° as suspected. The minimum receding contact angle of 112.6° is not far from 90° as the experimental observation had suggested. A similar statement can be made by reexamining Figure 2.5c, which is an image of an adhered bubble at equilibrium. The interface thickness can be seen to be uniform about

the entire perimeter showing no contact angle hysteresis. The interface shadow is quite thick suggesting substantial curvature and thus large contact angles. This is supported by this experiment in which the equilibrium contact angle was found to be 140.4°.

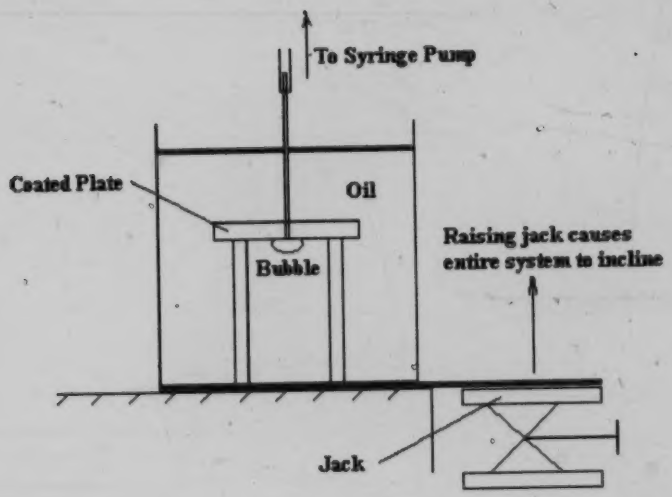

Figure 3.1 – Contact angle measurement apparatus

Figure 3.2 – Air bubble just prior to detachment

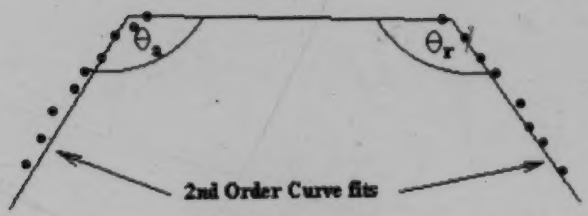

Figure 3.3 – Diagram of technique used to analyze digitized bubble images

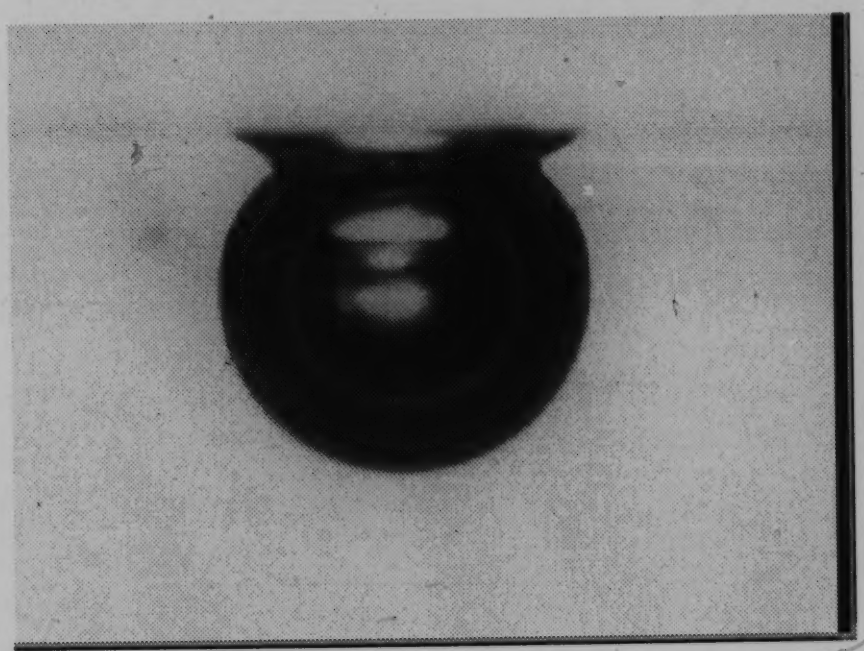

Figure 3.4 – Air bubble at equilibrium

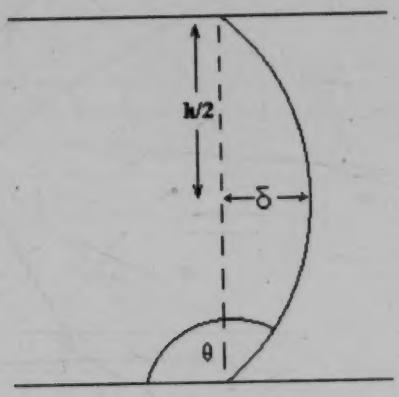

Figure 3.5 – Oil-air interface geometry assuming a circular interface profile

CHAPTER 4

LAPLACE EQUATION OF CAPILLARITY

4.1 MOTIVATION

A key approximation with regards to the modeling to follow in Chapter 5 is that the bubble's shape within the channel will be a cylinder. Inspection of the interface shadow present in the experiments indicates that the oil-air interface does have some curvature. For the bubble to approximated as a cylinder, this curvature must be small in comparison to the other bubble dimensions. The maximum advancing and receding static contact angle for a bubble of air submerged in MCT-30 on a FC-725 coated surface are 163.6° and 112.6° respectively as discussed in Chapter 3. The maximum receding contact angle is not far from 90° so it seems that approximating the oil-air interface from upper surface to lower surface as a vertical line should be a decent approximation on the upstream side of the bubble. The reasoning behind this statement was discussed in Section 2.3.3.1. The advancing contact angle is much closer to 180° however and it is not clear as to whether the downstream interface can be modeled as a straight line. The equilibrium contact angle was also found to be close to 180°. The quality of the straight interface approximation can be quantified by solving the Laplace equation of Capillarity for the interfaces to determine the deviation from the linear assumption. A small deviation with respect to the other bubble dimensions would allow the bubble to be modeled as a cylinder with small error with regards to shape. In this chapter, the methodology to solve the Laplace equation of Capillarity for the bubble interfaces

present in this work will be given. Solutions will be obtained for the interface profile using the extreme static contact angles and results interpreted in terms of the cylindrical bubble shape assumption.

The situation to be modeled is shown in Figure 4.1. This depicts the MCT-30/air interface inside a channel of height, h. The view is rotated 90° clockwise so that gravity is acting from right to left. At the solid surface the shape of the interface can be seen to make an angle θ' with the solid. In this case, θ' is the contact angle minus 90°. The left solid surface is labeled as x=0 and where the oil/air interface makes contact there is defined as y = R_c. Each of the maximum advancing and receding contact angles will be investigated separately. The reason for this is that the bubbles must be considered to be axisymmetric to apply the Laplace equation of Capillarity to the situation in an efficient manner. Thus the contact angles must be considered on an individual basis. The parameters varied in this numerical study were the channel height and the bubble contact radius.

4.2 LAPLACE EQUATION OF CAPILLARITY

The well known Laplace equation of Capillarity for this particular situation is

$$\Delta P = P_l - P_a = \gamma\left(\frac{1}{R_1} + \frac{1}{R_2}\right) \tag{4.1}$$

where P_a is the pressure on the air side, P_l is the pressure on the oil side, γ is the oil-air interfacial tension and R_1 and R_2 represent the principle radii of curvature of the interface. For any point on the oil-air interface, the static pressures are:

$$P_a = P_{a0} - \rho_a g x \tag{4.2}$$

$$P_l = P_{l0} - \rho_l g x \tag{4.3}$$

where ρ_a is the air density, ρ_l is the oil density, g is the acceleration of gravity and P_{oa} and P_{ol} are the reference pressures for the air and oil respectively at the lower surface(x=0). The reference pressures can be formulated by applying the Laplace equation of Capillarity to the interface at the lower surface. It can be shown that:

$$\Delta P_0 = P_{l0} - P_{a0} = \gamma\left(\frac{1}{R_{10}} + \frac{1}{R_{20}}\right) \tag{4.4}$$

where all terms are evaluated at the lower surface.

Substituting Equations 4.2-4.4, into Equation 4.1 and simplifying results in:

$$\gamma\left(\frac{1}{R_1} + \frac{1}{R_2}\right) = \gamma\left(\frac{1}{R_{10}} + \frac{1}{R_{20}}\right) - \Delta\rho g x \tag{4.5}$$

Introducing the expressions used by Gu and Li(1997) for the radii of curvature for an axisymmetric shape.

$$\frac{1}{R_1} = -\frac{\frac{d^2 y}{dx^2}}{\left[1 + \left(\frac{dy}{dx}\right)^2\right]^{\frac{3}{2}}} \tag{4.6}$$

$$\frac{1}{R_2} = -\frac{\frac{dy}{dx}}{y\left[1 + \left(\frac{dy}{dx}\right)^2\right]^{\frac{1}{2}}} \tag{4.7}$$

Where y is the radial distance from the axis of the bubble. Substituting Equation 4.6 and

Equation 4.7 into Equation 4.5 and doing substantial manipulation results in:

$$\frac{d^2y}{dx^2} = \left(\left[\frac{\frac{d^2y}{dx^2}}{\left(1+\left(\frac{dy}{dx}\right)^2\right)^{\frac{3}{2}}} + \frac{\frac{dy}{dx}}{y\left(1+\left(\frac{dy}{dx}\right)^2\right)^{\frac{1}{2}}}\right]\Big|_{x=0} + \frac{\Delta\rho g x}{\gamma} - \frac{\frac{dy}{dx}}{y\left(1+\left(\frac{dy}{dx}\right)^2\right)^{\frac{1}{2}}}\right).\left(1+\left(\frac{dy}{dx}\right)^2\right)^{\frac{3}{2}} \tag{4.8}$$

At x = 0, the measured contact angles and geometry show that the slope of the interface curve will be tan θ', and the value of y will be the bubble contact radius, R_c. Simplification yields:

$$\frac{d^2y}{dx^2} = \left(\left[\frac{\frac{d^2y}{dx^2}\Big|_{x=0}}{\left(1+\tan^2\theta'\right)^{\frac{3}{2}}} + \frac{\tan\theta'}{R_c\left(1+\tan^2\theta'\right)^{\frac{1}{2}}}\right] + \frac{\Delta\rho g x}{\gamma} - \frac{\frac{dy}{dx}}{y\left(1+\left(\frac{dy}{dx}\right)^2\right)^{\frac{1}{2}}}\right).\left(1+\left(\frac{dy}{dx}\right)^2\right)^{\frac{3}{2}} \tag{4.9}$$

In summary, $y=R_c$ at x=0 and x=h and the problem is well defined, non-linear, boundary value problem. This equation will be solved in an iterative manner.

4.3 SOLUTION TECHNIQUE

The domain 0 < x < h was divided into 501 equal divisions. This resulted in a one dimensional computational grid with 499 unknowns (the two boundary nodes are given as y = R_c). An index 'i' will number the unknowns from 0 at x=0 to 501 at x=h. Both the first and second derivatives were discretized with second order center differences, i.e,

$$\frac{dy}{dx} = \frac{y_{i+1} - y_{i-1}}{2\Delta x} + O(\Delta x^2) \tag{4.10}$$

$$\frac{d^2y}{dx^2} = \frac{y_{i+1} - 2y_i + y_{i-1}}{\Delta x^2} + O(\Delta x^2) \tag{4.11}$$

Replacing the corresponding derivatives in Equation 4.9 with the approximations in Equations 4.10-4.11 results in the following finite difference equation:

$$\frac{y_{i+1} - 2y_i + y_{i-1}}{\Delta x^2} = \left(\left[\frac{\left.\frac{d^2y}{dx^2}\right|_{x=0}}{(1+\tan^2\theta)^{\frac{3}{2}}} + \frac{\tan\theta}{R(1+\tan^2\theta)^{\frac{1}{2}}}\right] + \frac{\Delta\rho g x_i}{\gamma}\right.$$
$$\left. - \frac{\frac{y_{i+1} - y_{i-1}}{2\Delta x}}{y_i\left(1+\left(\frac{y_{i+1} - y_{i-1}}{2\Delta x}\right)^2\right)^{\frac{1}{2}}}\right).\left(1+\left(\frac{y_{i+1} - y_{i-1}}{2\Delta x}\right)^2\right)^{\frac{3}{2}} \tag{4.12}$$

To simplify the appearance of Equation 4.12, 'A' is defined to be equal to the right hand side of Equation 4.12. Substituting 'A' into Equation 4.12 and rearranging in such a manner that an iterative solution technique may be employed gives:

$$y_i = \frac{y_{i+1} + y_{i-1} - A\Delta x^2}{2} \tag{4.13}$$

In order to correctly formulate 'A' the second derivative evaluated at the x = 0 boundary must be dealt with. A second order forward difference approximation is:

$$\left.\frac{d^2y}{dx^2}\right|_{x=0} = \frac{2y_0 - 5y_1 + 4y_2 - y_3}{\Delta x^2} + O(\Delta x^2) \tag{4.14}$$

and this allows the second derivative at the lower surface to be evaluated to the same order as the remainder of the solution. This term must be calculated at the beginning of each iteration cycle as the solution will change with each iteration.

For each trial, the initial guess was a circular arc interface profile. This initial guess was found by analytically determining the circular arc that intersects the channel surfaces at

the contact angle to be investigated. Using the coordinate system of Figure 4.1, the equation of this arc can be shown to be:

$$y = R_c + [(\frac{1}{\tan^2\theta'} + 1)\frac{h^2}{4} - (x - \frac{h}{2})^2]^{\frac{1}{2}} - \frac{h}{2\tan\theta'} \qquad (4.15)$$

which is valid for $0 \le x \le h$.

It was decided to solve the equations by using the Gauss-Seidel iteration technique with a successive over-relaxation scheme. The optimal relaxation factor was determined empirically to be approximately 1.5. The convergence criterion was chosen as a relative change in the solution norm of less than 1×10^{-5}. A FORTRAN code was written to solve for the interface profile in the manner outlined in the preceding paragraphs. The code is available as Code 4.1 in Appendix A. The simulations were run on Pentium 200 PC with 16 MB of RAM without technical difficulty.

4.4 RESULTS

The model was solved with all possible combinations of h = 34, 60, 122, and 164 μm, R_c = 100, 200, 400, 800, and 1600 μm and with both advancing (θ = 163.6°) and receding (θ = 112.6°) contact angles for a total of 40 trials. The primary target of this investigation was the deviation from the desired linear assumption in terms of channel height and bubble radius.

Figure 4.2 is a plot of the interface profiles calculated for the channel height of h = 122 μm. The curves seem to be parabolic in nature but no attempt was made to prove this

with a curve fitting analysis. The maximum point on each curve represents the maximum deviation from the linear assumption that is desired. Clearly, the curve for the advancing contact angle deviates further than that for the receding contact angle. This was expected as the advancing contact angle is much larger than the receding contact angle (163.6° versus 112.6°). The data from the trials with the other channel heights showed similar results. In general the largest deviations were calculated at the larger channels and this will be quantified in the following section.

Figure 4.3 is a plot of maximum deviation versus channel height for various bubble contact radii. The relation between deviation and h (for a set R_c) is clearly a linear one. This makes sense intuitively as one would expect that the more space a bubble has to bulge outwards, the farther it will bulge outwards. The figure also demonstrates that the deviations dependence on the bubble contact radius, R_c, is very small. For h = 122 μm and θ = 163.6°, the deviation changed from 29.5 μm for R_c = 100 μm to 34.9 μm for R_c = 1600 μm. The curvature of the bubble interface due to the bubble contact radius is not an important factor.

The deviation from a linear assumption has to be compared to the other bubble dimensions to provide an insight to how effective the assumption of a linear interface profile will be. A sensible way to do this is to divide the maximum deviation calculated by the channel height. If a small deviation occurs over a large channel height then it would certainly justify the linear assumption. The results from this calculation were averaged for all R_c used (as R_c had no effect upon h and very little upon the magnitude of the deviation for each h) and multiplied by 100 to give a percentage deviation. The percentage deviation for all h and different contact angles are in Table 4.1.

With a maximum percentage deviation of 8.3% occurring at h = 34 μm, it is apparent that a vertical interface assumption is appropriate for the upstream side (receding contact angle side). However with a maximum percentage deviation of 28.3% for h = 34 μm with the advancing contact angle, it is unclear whether the same can be said regarding the downstream side of the bubble. A deviation of nearly one third the channel height is certainly significant when seen in this context. To determine the significance of the curvature of the interface with regards to computing a drag force the situation can be viewed from a different perspective. The other significant dimension in this problem is the diameter of the bubble. If the percentage deviation is recalculated considering the bubble contact diameter rather than the channel height, a different conclusion will be found. Table 4.2 lists the results of this computation for the advancing contact angle only. A small percentage deviation calculated in this manner will indicate that the interface deflection in comparison with size of the bubble will be negligible. From this data, the validity of the vertical interface assumption for the downstream side of the bubble can be checked. First, it seems that the assumption will be excellent for large bubbles as every percentage deviation computed for R_c>400 μm was less than 7%. Second, the larger values of h had consistently higher percentage deviations than the smaller channels. For instance, the percentage deviation for h = 164 μm with R_c=100 μm was 23.1% while the smallest channel, h = 34 μm, had a percentage deviation of 4.6% with this bubble radius. In general, the assumption of a vertical interface on the advancing contact angle side of the bubble cannot be entirely trusted for bubbles with R_c<400 μm in channels of h>=122 μm. It is a good assumption for the receding side of the bubble and is valid to some extent on the advancing side of the bubble. The limitations of the assumption for the

situation of smaller bubbles in the larger channels should be realized.

In Chapter 5, the results found here will be used to approximate the bubble cross-sectional shape as a cylinder. The approximation should be excellent on the upstream side for all bubbles. Limitations were found for combinations of small bubbles in larger channel heights for the downstream interface however.

The solution technique described here will be used in the following Chapter. The goal there, is to find the maximum deviation from a straight, vertical, interface as it was here. This deviation will be used to increase the contact diameter in order to comply with a model to be introduced later. The key modification to incorporate is that the contact angles used will vary with the Capillary number and channel height. This is easily incorporated in the solution as only θ' in Equation 4.12 needs to be changed. Equation 4.12 can accept any value for the contact angle and the interface profile can be obtained in exactly the same manner outlined in this Chapter.

Table 4.1a – Percentage Deviation in terms of channel height for θ_r

	R_c=100 μm	200 μm	400 μm	800 μm	1600 μm
h=34 μm	7.9%	8.2%	8.2%	8.2%	8.5%
60 μm	7.8%	8.2%	8.3%	8.3%	8.3%
122 μm	7.2%	7.8%	8.1%	8.3%	8.4%
164 μm	6.9%	7.6%	8.0%	8.2%	8.4%

Table 4.1b – Percentage Deviation in terms of channel height for θ_a

	100 μm	200 μm	400 μm	800 μm	1600 μm
h=34 μm	27.4%	28.2%	28.5%	28.8%	28.8%
60 μm	26.3%	27.5%	28.2%	28.7%	28.8%
122 μm	24.2%	26.2%	27.5%	28.1%	28.6%
164 μm	23.1%	25.6%	27.1%	28.0%	28.5%

Table 4.2 – Percentage Deviation in terms of bubble contact radius for θ_a

	R_c=100 μm	200 μm	400 μm	800 μm	1600 μm
h=34 μm	9.3%	4.8%	2.4%	1.2%	0.6%
60 μm	15.8%	8.3%	4.2%	2.2%	1.1%
122 μm	29.5%	16.0%	8.4%	4.3%	2.2%
164 μm	37.9%	21%	11.1%	5.8%	2.9%

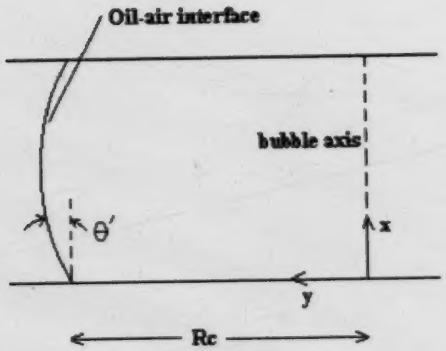

Figure 4.1 – Interface geometry setup

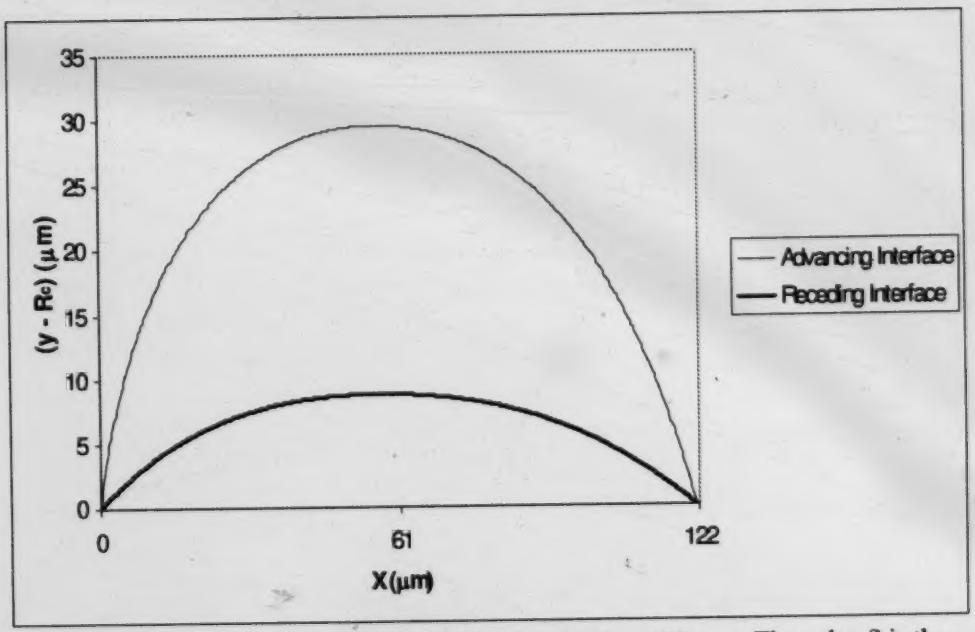

Figure 4.2 – Interface profiles for h=122 μm and R_c = 100 μm. The value δ is the maximum value of these curves.

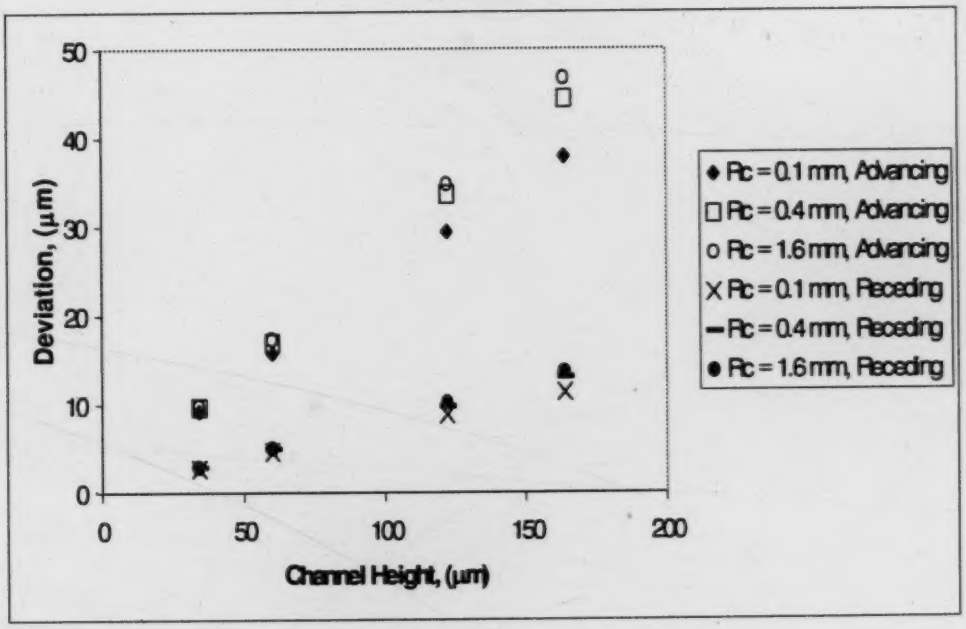

Figure 4.3 – Deviation versus h for various values of contact radius

CHAPTER 5

MODELING OF THE CRITICAL STATE

5.1 FLUID SHEARING FORCE

A model to predict the required Capillary number to detach the bubbles will involve two parts. Expressions for the drag force and the adhesion force must be derived. Setting the drag force to be equal to the adhesion force will allow the critical detaching flow characteristics to be calculated. In the following sections two different methods for estimating the shearing force on a bubble adhering to both surfaces of a slit microchannel will be obtained and discussed.

The deformation of the bubble during the experiment should be quantified before proceeding. A measure of the rigidity of the bubble's surface, while being sheared, is the Capillary number. Capillary numbers much less than unity mean that the surface tension in the oil-air interface will be dominant in comparison to the viscous forces present. The oil-air interface under this condition will tend to retain its shape while being subjected to the viscous shear force. This allows the bubble to be modeled as a solid particle(with regards to shape) and simplifies the situation. The Capillary numbers at the critical states in the experiment were all much less than unity. The maximum value encountered in the experimentation was approximately $Ca_{cr} = 0.006$.

5.1.1 Drag Force 1 - Underestimate

To begin, an expression that should give an underestimation of the drag force will be developed. A characteristic of flow through slit microchannels is that very large pressure gradients exist with relatively small flow rates. This can be seen by examining the Poiseuille flow equation as given in Equation 2.1. The pressure gradient inside a slit microchannel is proportional to $1/h^3$. This means that when the channel height is decreased to the order of several hundred micrometers as in this study, the pressure gradient will increase dramatically. This leads to the assumption that any viscous drag on the bubble will be negligible in comparison to the pressure drag on the bubble. An approximation of pressure drag on the bubble is to multiply the pressure drop across the bubble with the bubble frontal area.

$$F_{d(1)} = (\Delta P_{bubble})(A_f) \tag{5.1}$$

In Chapter 4, the Laplace Equation of Capillarity was solved to determine if the oil-air interface could be approximated as being vertical. For the extreme value of the receding air contact angle, the deviation of the interface from a vertical line was shown to be small for all values of h and D_c. The extreme advancing air contact angle solutions showed the vertical line assumption to be valid for small values of h and larger values of D_c. In any event, the small deviations will not significantly alter the bubble's frontal area. Proceeding with the vertical interface assumption and thus approximating the bubble as a rigid cylinder gives the frontal area as:

$$A_f = D_c h \tag{5.2}$$

which can be substituted into Equation 5.1. The pressure drop across the bubble will be a

difficult term to evaluate. For the majority of the experimental points the bubble diameter was small in comparison with the channel width. It is reasonable to believe then, that the pressure gradient across the bubble should be close to the theoretical Poiseuille pressure gradient from Equation 2.1. Accordingly, the pressure drop across the bubble can be written as:

$$\Delta P_{bubble} = \frac{12Q\mu D_c}{Wh^3} \tag{5.3}$$

However, using this pressure drop will give a value that is too small. The insertion of a rigid cylinder will significantly alter the flow field and the pressure gradient. The presence of an obstructing cylinder forces the flow around the cylinder. This increases the resistance to flow and in general it causes larger pressures than could be expected in an unobstructed channel. Intuitively, it is possible to state that the pressure gradient in the vicinity of the bubble will be larger than that predicted by a fully developed Poiseuille flow, but this is difficult to quantify further. In lieu of a complete three dimensional numerical simulation, this approximation will be made with the realization that the drag force expression will be an underestimate. Substituting Equation 5.2 and Equation 5.3 into Equation 5.1 results in:

$$F_{d(1)} = \frac{12Q\mu D_c^2}{Wh^2} \tag{5.4}$$

Replacing the flow rate, Q, with U_mhW gives:

$$F_{d(1)} = \frac{12U_m\mu D_c^2}{h} \tag{5.5}$$

where U_m is the average fluid velocity. Equation 5.5 shows that the larger the bubble contact diameter the larger the drag force, which makes sense physically. A larger bubble has more

surface area on which drag forces can act and should experience a greater drag force. It is interesting to note that the drag force is inversely proportional to h. It may seem that this is in error, as a cylinder in a small channel will have a smaller surface area on which drag forces can be imparted. This is reconciled by noting that the magnitude of the pressure gradient in the channel is inversely proportional to h^3. Therefore, the pressure drop across the bubble increases faster than the surface area on which it acts can decrease as h decreases. The net effect is larger drag forces on bubbles in small channels.

There are many reasons that Drag Force 1 will not produce an accurate value. As discussed above, Equation 5.5 is an estimation of the drag force on a bubble inside a channel but is derived with the pressure gradient expected in channel flow without any obstructions. This is clearly incorrect and will give too small a value for the pressure gradient in the bubble's vicinity. The omission of an analysis for a viscous drag force will also make this approximation err on the small side. However, this omission should cause a small error only due to the extremely small velocities to be considered. The viscous drag is proportional to the velocity of the flow and in this study the flow velocity was extremely small as shown by the extremely small values for the experiment Ca_{cr}. In any case, Drag Force 1 can be useful if it is realized that it is an underestimating formulation.

5.1.2 Drag Force 2 - Overestimate

To improve the formulation for the drag force, the work of Goldman(1967) can be used. In this work, the drag force on a translating sphere in simple shear flow near a horizontal surface is found by numerically solving the Stokes equations. A schematic of the

situation modeled is in Figure 5.1. The assumptions inherent in this solution are that the Reynold's number is small and that the flow field is unchanging in the direction perpendicular to the flow direction. The experimental Reynolds number in Chapter 2 were much smaller than unity with the largest value being approximately 0.01, thus meeting that requirement. The large aspect ratios (W/h) of the slit microchannels in the experiment makes the assumption of Poiseuille flow an excellent approximation as well. This was discussed in Section 2.4. Goldman(1967) found that the solution for the limiting case of the sphere tangent to the horizontal surface is:

$$F_d = 1.7\pi\mu SD^2 \tag{5.6}$$

where S is the shearing rate of the fluid. This result has been used in the work of Mahe et al.(1988) and Basu et al.(1997) to estimate the drag force on droplets with large contact angles with success. The shape of the experimental bubbles in this study were not spherical as required by Equation 5.6. In general, the shape of the bubbles closely resembled narrow cylinders rather than spheres. The difference in geometry is depicted in Figure 5.2. The effect of this difference in shape will be to predict too large a drag force. The diameter of the cylinder, D_c, will be inputted into Equation 5.6, which accurately gives a drag force for a sphere of diameter D. Clearly, the surface area of the cylinder(πD_c*h) will be smaller than the corresponding sphere(πD_c^2), thus the result for the drag force will be an overestimate(the ratio of sphere surface area to cylinder surface area can be shown to be D_c/h which was always large in the experiments). Another physical difference is that the experimental bubbles were subjected to a parabolic velocity profile in comparison to the linear velocity profile studied by Goldman. Mahe et al.(1988) and Basu et al.(1997) also encountered this difficulty,

but were able to work around it because the droplets in their studies were small in comparison to the channel height. Mahe and Basu could simply consider the shear rate at the channel wall as the shear rate acting on the droplet. In essence, the droplets in those studies were subjected to a linear shear flow because the droplets were not large enough to 'see' the parabolic nature of the velocity profile. In the present work, the air bubbles are large enough to span the entire height of the channel and thus will encounter the parabolic velocity. It is necessary then, to find an equivalent shear rate for a parabolic velocity profile and quantify what effects this deviation will have on the model. Consider a parabolic velocity profile in a channel of height, h, with a maximum velocity of U_{max} at z = h/2:

$$U(z) = \frac{4U_{max}}{h^2} z(h - z) \tag{5.7}$$

Equation 5.7 can readily be seen to satisfy the boundary conditions of u = 0 at z = 0 and z = h. The shear rate is then the first derivative of the velocity profile with respect to z.

$$S(z) = \frac{4U_{max}}{h^2} (h - 2z) \tag{5.8}$$

Equation 5.8 shows that the shear rate varies from a positive value at z = 0 to an equivalent magnitude negative value at z = h. This implies an average shear rate of zero, which is clearly not a useful result. It is more sensible to find the average absolute value of the shear rate. Taking advantage of the symmetry in the shear rate profile, the average shear rate can be found by integrating the shear rate over half the channel height, i.e.,

$$S_{ave} = \frac{2}{h} \int_0^{\frac{h}{2}} S(z) dz \tag{5.9}$$

It can be shown that the average absolute value of the shear rate will be:

$$S_{ave} = \frac{2U_{max}}{h} \tag{5.10}$$

The value of U_{max} is not a convenient quantity so it will be converted to the average velocity by integrating the velocity profile and dividing by h:

$$U_m = \frac{1}{h}\int_0^h U(z)dz \tag{5.11}$$

which results in:

$$U_m = \frac{2}{3}U_{max} \tag{5.12}$$

Substitution of Equation 5.12 into Equation 5.10 results in the following expression for the average shear rate:

$$S_{ave} = \frac{3}{h}U_m \tag{5.13}$$

It is necessary to know how the average shear rate for a parabolic velocity profile compares to the shear rate for a simple linear profile. Both profiles (with identical volumetric flow rates) will be compared in terms of the average shear rates. This computation will allow the validity of this approach to be quantified. Consider first a linear profile with a volumetric flow per unit width of Q and a constant shear rate S, and therefore a velocity relation u(z) = Sz. The velocity at a distance z = h is u = Sh. The flow rate can easily be shown to be:

$$Q_{shear} = \frac{1}{2}S_{shear}h^2 \tag{5.14}$$

and rearranging gives:

$$S_{shear} = \frac{2Q_{shear}}{h^2} \tag{5.15}$$

For a parabolic profile with an average velocity of U_m it is straightforward to show that:

$$Q_{parabolic} = U_m h \tag{5.16}$$

incorporation of Equation 5.16 into Equation 5.11 and manipulating gives:

$$S_{parabolic} = \frac{3Q_{parabolic}}{h^2} \tag{5.17}$$

Now for the same flow rate, the shear rate for a parabolic profile will be 1.5 times larger than that for a linear shear flow. By using the average shear for a parabolic profile instead of the expected linear shear rate, the outputted drag force will increase by 50% for the same value of Q. Therefore, having Poiseuille flow rather than shear flow will increase the drag on the bubble and make the removal of the attached bubbles easier.

Now that the average shear rate has been computed and its effect quantified, it can be substituted (Equation 5.11) into Equation 5.6 which results in:

$$F_{d(2)} = \frac{7.65\pi\mu D^2 U_m}{h} \tag{5.18}$$

It is noteworthy that both Drag Force 1 (Equation 5.5) and Drag Force 2 (Equation 5.18) are of the same form. They are both proportional to the product of $\mu U_m D_c^2$ and inversely proportional to h. The multiplying constant does change however. For the underestimating Equation 5.5, the constant has a value of 12. The constant for the overestimating Equation 5.18 has a value of 7.65π. It is interesting to realize that the division

of Equation 5.18 by Equation 5.5 results in a quotient of 2.00. Whether this is coincidental or is physically meaningful is not known.

At this point adjustment to Drag Force 2 is necessary. The diameter of the bubble is not the same as the bubble's contact diameter that was recorded during the experimental stage. In order to correct this small error the Laplace Equation of Capillarity can be solved as it was in Chapter 4. The methodology for solving this equation is exactly the same as described in Chapter 4, but the contact angles will have an extra degree of freedom. As will be discussed in the next section, the dynamic contact angles will be a function of the capillary number and channel height. These angles will change over the course of the experiment and must be accounted for. As explained in Chapter 4, the value of δ is the output from the solution of the Laplace Equation of Capillarity. To relate the bubble contact diameter to the actual bubble diameter, simply add the two values of delta to the contact diameter:

$$D = D_c + \delta_a + \delta_r \tag{5.19}$$

Where δ_a and δ_r are the maximum deviations from vertical for an axisymmetric interface in a channel of height h, contact diameter D_c, and dynamic contact angles of θ_a and θ_r respectively. The shearing force becomes:

$$F_{d(2)} = \frac{7.65\pi\mu(D_c + \delta_a + \delta_r)^2}{h} \tag{5.20}$$

Drag Force 1 (Equation 5.5) and Drag Force 2 (Equation 5.20) represent the lower and upper limits of what the drag force on the bubble should be. It is not obvious which expression is more accurate. It makes sense to retain both formulations and combine them with a weighted average. The relative weights given to each limit will be kept and used as

a tuning factor to adjust the model when comparing to the experimental data. Defining relative weights of W_1 and W_2 to the underestimating and overestimating formulations respectively:

$$F_d = W_1 \frac{12\mu D_c^2}{h(W_1+W_2)} + W_2 \frac{7.65\pi\mu(D_c+\delta_a+\delta_r)^2}{h(W_1+W_2)} \tag{5.21}$$

5.2 ADHESION FORCE

The source of the adhesion force is the surface tension of the oil-air interface and the contact angle hysteresis as discussed in Chapter 1. It was shown there that the interfacial force for a sessile drop is the surface tension integrated about the contact perimeter. This force will act in a direction that is specified by the contact angles formed with the surface. A typical equilibrium sessile drop forms a contact angle, θ, with the surface which does not change along the drop contact perimeter. A calculation of the net horizontal force on this drop would be zero as the contact angle is the same everywhere.

When an external horizontal force is applied to the drop it will deform locally in the region of the contact perimeter. The contact angles will shift to become different values along the contact perimeter. The difference in contact angles is known as contact angle hysteresis. Now a computation of the net horizontal interfacial force will be non-zero. The adhesion force from the contact angle hysteresis will act to counter the external force and resist motion.

How the contact angles change along the contact perimeter is a complex subject and

is not well resolved. There are several common assumptions made in literature. A general expression for the adhesion force is the integral of the component of surface tension that is parallel to the external force. Rewriting Equation 1.18 here:

$$F_a = \int \gamma \cos\theta \cos\eta \, R \, d\eta \tag{5.22}$$

where θ may be dependent upon η. It is common practice to assume that the contact angles on both the downstream and upstream side of the bubble have distinct, constant values. This results in Equation 5.22 evaluated to:

$$F_a = 2 R_c \gamma (\cos\theta_r - \cos\theta_a) \tag{5.23}$$

This is the formulation used by Mahe et al.(1988). In the study by Basu et al.(1997) a different assumption about the contact angle variation was assumed and the following adhesion force was found:

$$F_a = \frac{4}{\pi} R_c \gamma (\cos\theta_r - \cos\theta_a) \tag{5.24}$$

Another possible assumption to make is that the upstream contact angle varies linearly with η and the downstream contact angle remains at a constant value. The results of the integration for this situation is:

$$F_a = 2 R_c \gamma \left(\cos\theta_r - \frac{\frac{2}{\pi}(\theta_a - \theta_r)\sin\theta_a - \cos\theta_r}{\frac{4}{\pi^2}(\theta_a - \theta_r)^2 - 1}\right) \tag{5.25}$$

A decision must be made regarding which assumption is the most applicable to the bubbles in this experiment. Examining the images presented in Chapter 2, (Figure 2.9a and Figure 2.9b), an educated guess as to how the contact angles are behaving along the contact

perimeter can be made. In both Figure 2.9a and Figure 2.9b, the curvature of the oil-air interface is visible as the thickness of the shadow about the perimeter. A wide line shows that the interface is bowing outwards more, while a thin line shows that the interface is nearly vertical. As explained in Section 2.3, and from the results from solving the Laplace Equation of Capillarity in Chapter 4, a large amount of curvature in the oil-air interface is representative of a large contact angle. From these images it is evident that the downstream contact angles are significantly larger than the upstream contact angles. Examining the variation of the thickness of the interface shadow along the bubble contact perimeter will allow the relationship between the contact angles and position on the contact perimeter to established. The interface thickness does seem to remain constant for the entirety of the upstream side. When the point on the perimeter is reached when the perimeter is parallel to the flow direction a sudden jump is seen in the interface thickness. After this sudden change the thickness remains constant about the majority of the downstream side. If there is any variation along the upstream perimeter it seems to be small and would be difficult to quantify from these observations alone. The observations put forth here justify assuming the contact angles are constant on the upstream and downstream sides and thus Equation 5.23 would be the formulation to use. A small modification is necessary to account for the additional surface of contact in this case. Equation 5.23 governs a bubble attached to a single surface but in this study the bubble is attached to two(upper and lower channel surfaces). Multiplying by a factor of two results in:

$$F_a = 2 D_c \gamma (\cos\theta_r - \cos\theta_a) \tag{5.26}$$

That the dynamic contact angles are dependent upon the Capillary number,

equilibrium contact angles, and microscopic and macroscopic length scales must be considered. As described in Chapter 1, the contact angles for a moving interface are called dynamic contact angles. To predict the onset of motion the dynamic contact angles must be estimated and used in Equation 5.26.

Cox(1986) studied the motion of a three phase line in flow where the Reynold's and Capillary numbers are much smaller than unity. The situation is depicted in Figure 5.3. The solution involves specifying a slip length, s, near the dynamic contact line to solve the Stokes equation with matched asymptotic expansions. The results from Cox's analysis are summarized by Basu et al.(1997) in the following set of equations:

$$g(\theta_a,\lambda) = g(\theta_e,\lambda) + Ca\ln(\varepsilon_s^{-1}) + O(Ca)$$

$$g(\theta_i,\lambda) = \int_0^{\theta_i} \frac{d\beta}{f(\beta,\lambda)}$$

$$f(\beta,\lambda) = \frac{2\sin\beta[\lambda^2(\beta^2-\sin^2\beta)+2\lambda(\beta(\pi-\beta)+\sin^2\beta)+((\pi-\beta)^2-\sin^2\beta)]}{\lambda(\beta^2-\sin^2\beta)[(\pi-\beta)+\sin\beta\cos\beta]+[(\pi-\beta)^2-\sin^2\beta](\beta-\sin\beta\cos\beta)}$$

$$Ca = \frac{\mu_{oil}U_m}{\gamma_{lv}}$$

$$\lambda = \frac{\mu_{air}}{\mu_{oil}}$$

$$\varepsilon_s = \frac{s}{L_m} \qquad (5.27)$$

where λ is the ratio of the viscosities of the displaced fluid and displaced fluid, Ca is the

capillary number based on average shearing velocity and the viscosity of the displacing fluid, s is a microscopic length scale, L_m is a macroscopic length scale, and θ_e is the contact angle measured from the displacing fluid side as shown in Figure 5.3. The formulae in Equation 5.27 govern the moving interface as the oil phase displaces the air phase, i.e., the bubble's receding contact angle. To model the air phase displacing the oil phase (the air advancing contact angle), simply use λ^{-1} in place of λ in the formula for $f(\theta_i)$, λCa in place of Ca, and $\pi-\theta_e$ in place of θ_e. The obvious choice for the macroscopic length scale is the channel height, h. The microscopic slip length is harder to quantify. Other research into drop spreading (Gu and Li, 1998, Basu et al., 1996) has found 's' to range from 1-5 μm. It is not well understood why the slip length should fall in this range for most experimental data.

The study of Cox into the motion of the three phase contact line reveals that the dynamic contact angles are dependent upon the capillary number and the channel height. The function $g(\theta)$ can be found numerically for any value of λ. In this study the values of the viscosity ratio are $\lambda = 5.95 \times 10^{-5}$ and $\lambda^{-1}=16800$. The function $g(\theta)$ was computed for these values of λ and the result is given as Figure 5.4. The curves are consistent with the results presented by Cox.. The integration was performed using Simpson's Rule with 1000 function evaluations. The Fortran code used is available as Code 5:1 in Appendix A. With these curves, one can find $g(\theta)$ for any value of θ, and θ from a value of $g(\theta)$. The procedure then to determine the air receding contact angle is to determine $g(\theta_e)$, shift along the abscissa of Figure 5.4 a distance of $Ca*\ln(h/s)$ to the right and read θ_r from the ordinate. The procedure is the same for the advancing air contact angle, but the proper quantities must be substituted

as outlined earlier.

The validity of this approach is questionable for combinations of large values of θ_e (or π-θ_e) and large values of λ (or λ^{-1}). This is discussed by Cox(1986) and can be seen by examining Figure 5.4. For the advancing contact angle, the curve for λ=16800 must be used. For the equilibrium contact angle of 140.4°, $g(\theta_e)$ =2.7437x10^{-4}, and g(180°) = 2.76604x10^{-4}. To obtain the advancing dynamic contact angle, move along the abscissa to the right a distance of Ca*ln(h/s) from $g(\theta_e)$ and find $g(\theta_a)$ from the ordinate. Since physically, the advancing contact angle cannot exceed 180°, the value of g(180°) cannot be exceeded either. This gives very little room along the abscissa to move and puts a limit on how large a capillary number can exist before invalidating Cox's method. The maximum value of Ca can be solved for as follows:

$$Ca \ln(h/s) \leq g(\theta_e) - g(180^0) \tag{5.28}$$

Using a value for the microscopic slip of 1 μm and solving for the maximum valid Capillary number reveals that the experimental Capillary numbers are well outside the valid range. The largest valid Capillary numbers are 0.0105, 0.0090, 0.0077, and 0.0072 for the channel heights of 34, 60, 122, and 164 μm respectively. By examining the curve for λ = 5.95x10^{-5}, it is clear that there is no such problem for the receding contact angle and Cox's method can be applied.

Another formulation to handle the advancing air contact angle must be found. The results from Chapter 3, where the extreme values of the dynamic advancing and receding contact angles were determined experimentally, can be used. The maximum static advancing

contact attainable was found to 163.6° ± 3.6°. Though Cox's analysis cannot successfully be utilized in this case, the patterns identified may be of some help. For a situation of Ca*ln(h/s) = 0, the contact angle will not change from its equilibrium value. As Ca*ln(h/s) increases, the advancing contact angle should increase monotonically as per Figures 5.4. The maximum value this angle can achieve is 163.6° and the minimum is the equilibrium value of 140.4°. Since the angle must continually increase with Ca*ln(h/s), the advancing contact angle should asymptotically approach the value of 163.6° as the product Ca*ln(h/s) increases. The behavior of the advancing contact angle will thus have to be approximated using the following criterion:

$$\begin{aligned} Ca\ \ln(h/s) &= 0,\ \theta_a = 140.4^\circ \\ Ca\ \ln(h/s) &\to \infty,\ \theta_a \to 163.6^\circ \end{aligned} \tag{5.29}$$

It is not clear exactly how the dynamic advancing air contact angle should behave to satisfy these conditions. At a later time, this function will be adjusted to improve the modeling accuracy. The empirically determined behavior of θ_a will have to checked to ensure that it obeys the conditions set up in Equation 5.29.

5.3 DETERMINATION OF THE CRITICAL STATE

The critical state will be found when the drag force is equal to the adhesion force. Equating Equation 5.21 and Equation 5.26 results in:

$$W_1 \frac{12\mu D_c^2 U_m}{h(W_1+W_2)} + W_2 \frac{7.65\pi\mu (D_c+\delta_a+\delta_r)^2 U_m}{h(W_1+W_2)} = 2\gamma D_c(\cos\theta_r - \cos\theta_a) \quad (5.30)$$

To be consistent with the experimental results presentation, Equation 5.30 can be manipulated to solve for the critical capillary number.

$$Ca_\sigma = \frac{2(\cos\theta_a - \cos\theta_r) D_c h(W_1+W_2)}{12 W_1 D_c^2 + 7.65\pi W_2 (D_c+\delta_a+\delta_r)^2} \quad (5.31)$$

where θ_a and θ_r depend on h and Ca as per Cox's(1986) formulation, and δ_a and δ_r depend upon θ_a, θ_r, h, and D_c as per Laplace's Equation of Capillarity. A specialized numerical technique to solve Equation 5.31 is required as both sides of the equation have dependence upon Ca and it is not possible to simplify further.

5.3.1 Solution Technique

The model given in the preceding paragraphs must be solved in an iterative manner. Most terms given in Equation 5.31 have a complex dependence upon Ca, h, and D_c. Keeping the form given in Equation 5.31, the solution procedure can be organized such that the Capillary number may be solved for with a fixed-point iteration technique.

The algorithm for this iterative technique is as follows: First an initial guess for the Capillary number is made. With this guess the receding dynamic air contact angle can be evaluated via Cox's method and adjusting the advancing air contact angles to fit the data. The assumed values for the advancing air contact angle will be checked later to ensure they make sense physically. With these contact angles, the Laplace equation of Capillarity can be solved as shown in Chapter 4 and the quantities δ_a and δ_r can be evaluated. These quantities

can relate the actual bubble diameter to the bubble contact diameter and the right hand side of Equation 5.31 can be fully evaluated. The capillary number arrived at becomes the next initial guess and the process is repeated until convergence. The initial guess was determined from examining the experimental data. An inital guess of Ca=0.001 was used for all cases. The iterations continued until a relative change of less $1x10^{-5}$ was observed in Ca. This algorithm is available as Code 5.2 in Appendix A. The code was run for $2<D_c/h<20$ and for all channel heights. The weighting averages were handled by simply setting $W_1=0$ and $W_2=1$ and solving and then setting $W_1=1$ and $W_2=0$ and solving. This resulted in 2 sets of data representing the upper and lower limits of the drag force formulation. The microscopic slip length was set to a value of 1 μm as per most of the literature values.

5.4 MODEL RESULTS

For each channel height the modeling results were compared to the experimental data. Figures 5.5-5.8 show the upper and lower limits (corresponding to Drag Force 1 and 2) of the modeling Ca_{cr} plotted on the same graph as the experimental values for each channel height. The error bars are the average errors found from the uncertainty analysis in Chapter 2.

5.4.1 Model predictions compared to experimental data

The model prediction for h=34 μm is shown in Figure 5.5. The experimental data showed a small negative slope as the D_c/h ratio increased. The modeling seems to do a good

job with showing this as well. It can be seen that the experimental data points mostly fall between the two theoretical curves. The exceptions are the two points nearest $D_c/h=1$. Small ratios of D_c/h will be shown to disagree with theory for nearly every channel height. A possible explanation of this is shown in Figure 5.9. As a bubble becomes smaller in volume, it has less tendency to be adhered to both surfaces. It will be more likely to completely detach from one surface and form a sessile drop on the other. The modeling, however, does not take this into account. The model assumes that as the bubble shrinks it will always remain firmly attached to both surfaces with the same contact angles as a large volume bubble would have. However, the bubble will physically become more spherical and less cylindrical as the bubble volume decreases. This will cause the adhesion force to become weakened, as the contact angles will approach 180 degrees on both sides of the bubble. That is, as h approaches the value of D_c, a spherical bubble will just be able to make contact with both surfaces. The model does not consider this potential change in bubble geometry. It considers only that the bubble must remain cylindrical in the limit of h going to D_c. This is demonstrated in Figure 5.10. This shows what the model is approximating as the bubble volume gets small. The needle shaped bubbles shown are clearly not what should happen physically. The set of images in Figure 5.9 is far more likely to occur and it is intuitive that this should be the expected behavior of a shrinking bubble. This is the source of the discrepancies for D_c/h near unity. In fact, at $D_c/h = 1$, it is not clear as to whether the problem description holds as the bubbles do not have sufficient volume to be able to adhere to both surfaces of a microchannel. For $D_c/h < 1$, a bubble will not be able to adhere to both channel surfaces and the nature of the problem changes dramatically. In any event, the model does well for the larger values of

D_c/h where the vast majority of the experimental points exist.

The theoretical curve for a channel height of 60 μm is compared to the experimental data in Figure 5.6. As for the 34 μm channel, the theoretical curves do an excellent job of defining the range of expected shearing forces at larger values of D_c/h. Again, both theoretical curves begin to perform badly as D_c/h approaches unity for the same reasons outlined in the previous paragraph. The experimental results at this channel height showed a small negative slope and this is in agreement with the theoretical modeling. The model predicts that the critical capillary numbers should be larger than for the h=34 μm channel results which is in agreement with the experimental results.

Figure 5.7 compares the theoretical predictions to the experimental data for h=122 μm. The two theoretical curves can be seen to predict the range in which most of the data falls very well. Again, discrepancy is found for values of D_c/h near unity. In comparison to the other channels, the model predicts a much larger slope as D_c/h increases as was shown in the experimental results. As expected, the critical capillary numbers are, in general, larger than those for channels with smaller values for channel height.

Figure 5.8 compares the modeling results to the experimental data for h=164 μm. Again, the theoretical model does an excellent job of describing where the experimental data will fall at larger values of D_c/h. The discrepancy at D_c/h values near unity is once again present. The slope of the curves becomes larger as h increases from 122 μm to 164 μm as the experimental data suggests. The model also predicts larger critical capillary numbers at similar values of D_c/h for this channel in comparison to the smaller channels.

5.4.2 Dynamic Advancing Air Contact Angle Estimation

The results presented in this section are dependent upon the estimated function that the dynamic advancing air contact angle obeys. For each channel height, the value for θ_a that best fits the experimental data was chosen. A plot of the best θ_a versus h is given in Figure 5.11. The behavior of the curve is that it increases at a moderate rate from the equilibrium contact angle. The maximum value of $\theta_a = 156°$ was found at the largest channel height. That the maximum value of θ_a was found to be less than the maximum possible dynamic advancing contact angle of 163.6° means that the values of θ_a that agree best with the experimental are within its physical bounds.

5.5 MODEL PERFORMANCE

The model provided in this chapter uses two formulations for the drag force. One formulation was shown to be an underestimate and the other was shown to be an overestimate. Together, they define a range in which the actual drag force is expected to fall. Equating the drag force to a model for the adhesion force, and accounting for the variation of the receding contact angle with the Capillary number and channel dimensions, completed the model. The advancing dynamic contact angle was adjusted for each channel height to fit the experimental data. The behavior of the empirically determined function for θ_a increases from the equilibrium contact angle towards the maximum static advancing contact angle. The behavior of θ_a with channel height is acceptable from a physical standpoint as it obeys the boundary conditions given in Equation 5.29.

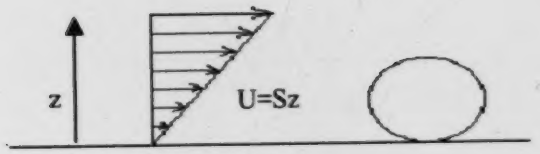

Figure 5.1 – Sphere tangent to a wall in shear flow

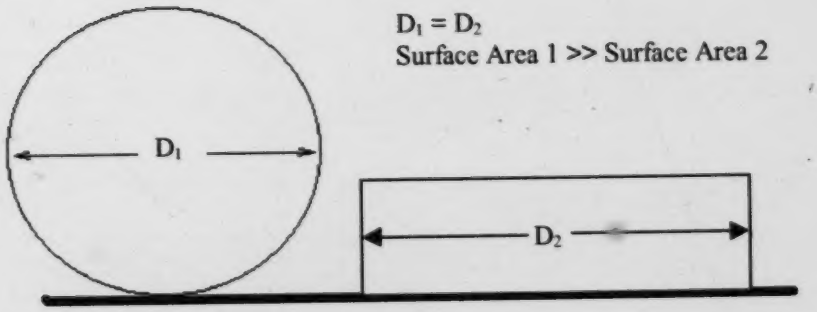

Figure 5.2 – Geometrical differences between experimental and modeling bubbles

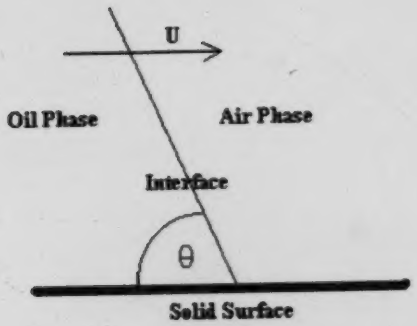

Figure 5.3 – Diagram of a moving oil-air interface across a solid surface

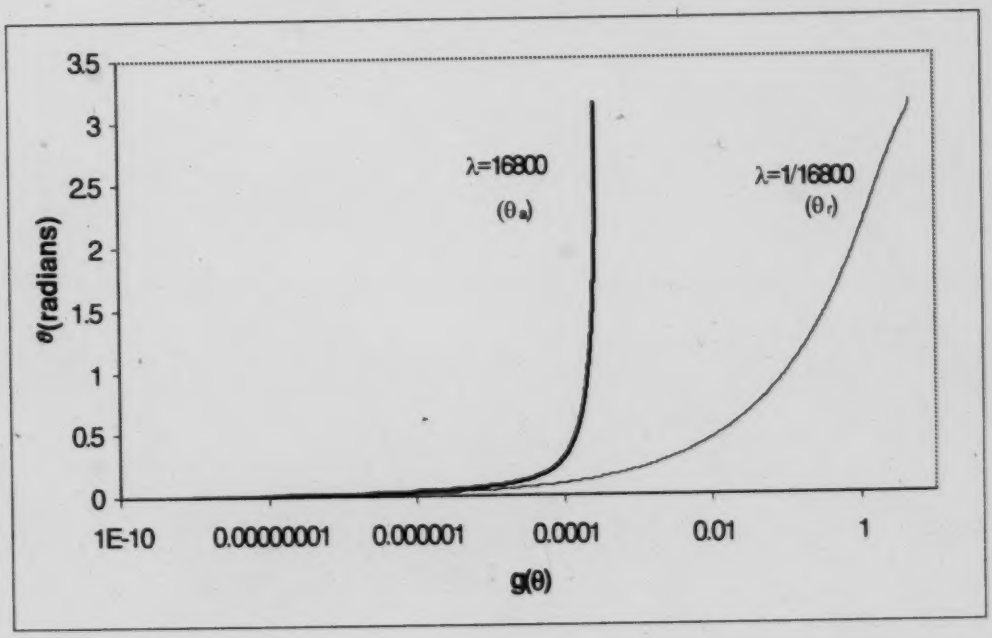

Figure 5.4 –Solution of Cox's Model for advancing and receding contact angle

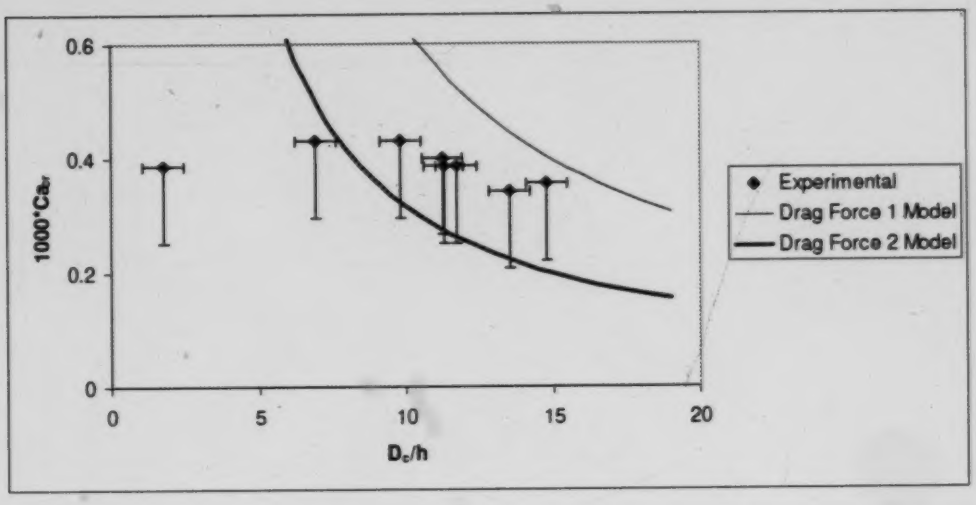

Figure 5.5 – Modeling results for h=34 μm

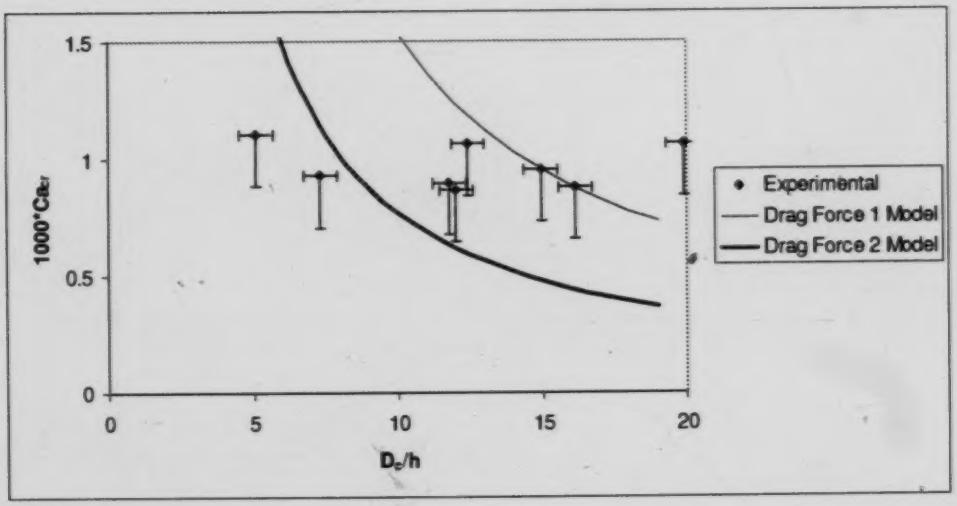

Figure 5.6 – Modeling results for h=60 μm

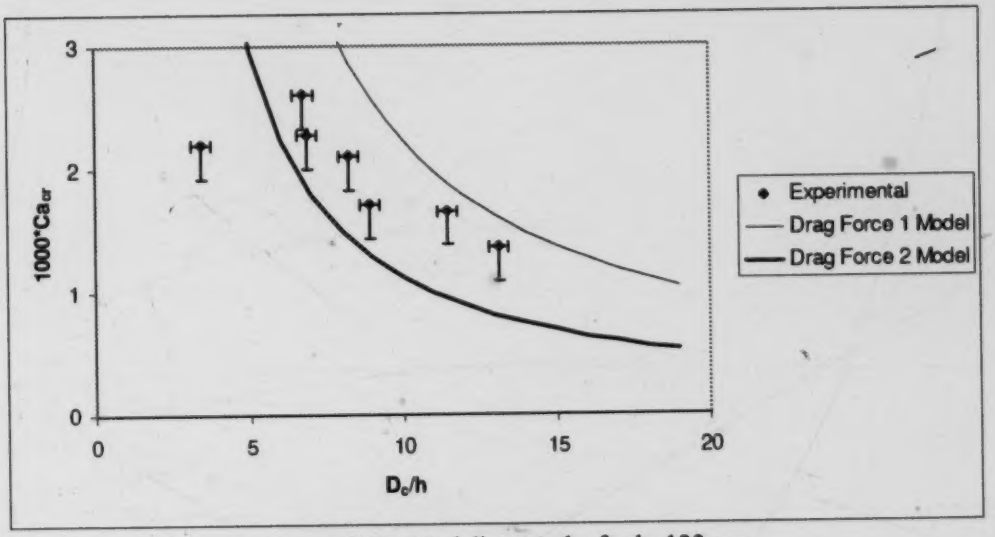

Figure 5.7 – Modeling results for h=122 μm

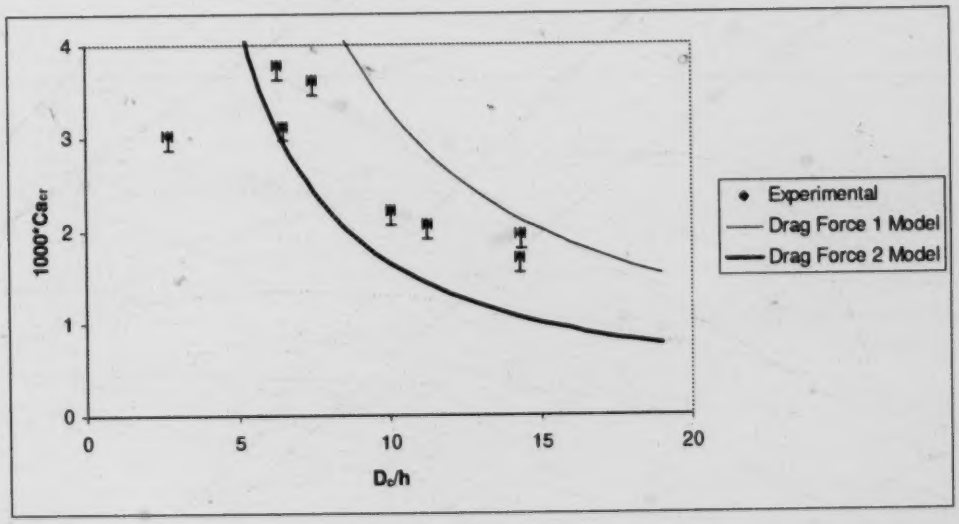

Figure 5.8 – Modeling results for h=164 μm

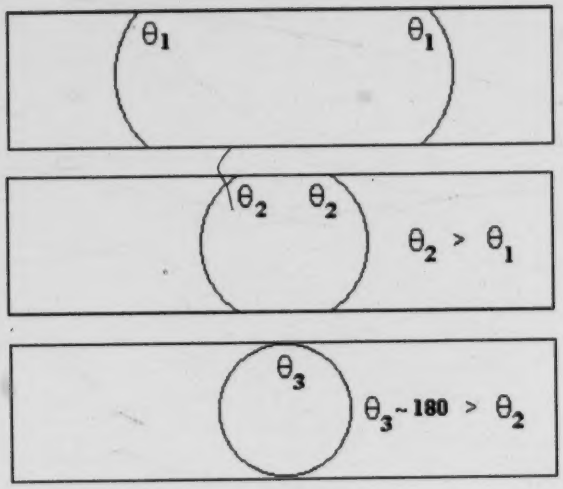

Figure 5.9 – Unaccounted for contact angle variation with D_c as D_c/h approaches unity

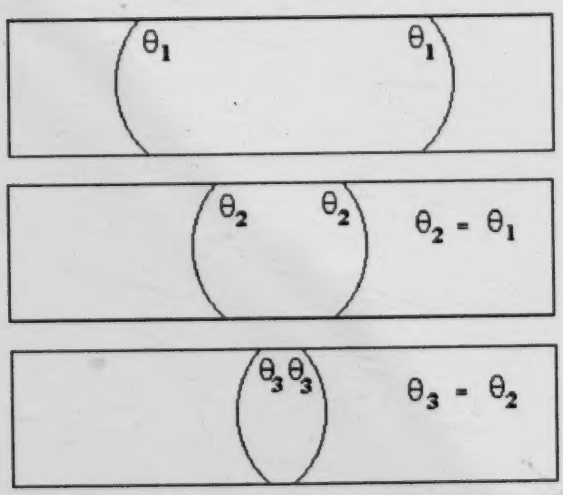

Figure 5.10 – Sketch of model's handling of contact angles as D_c decreases

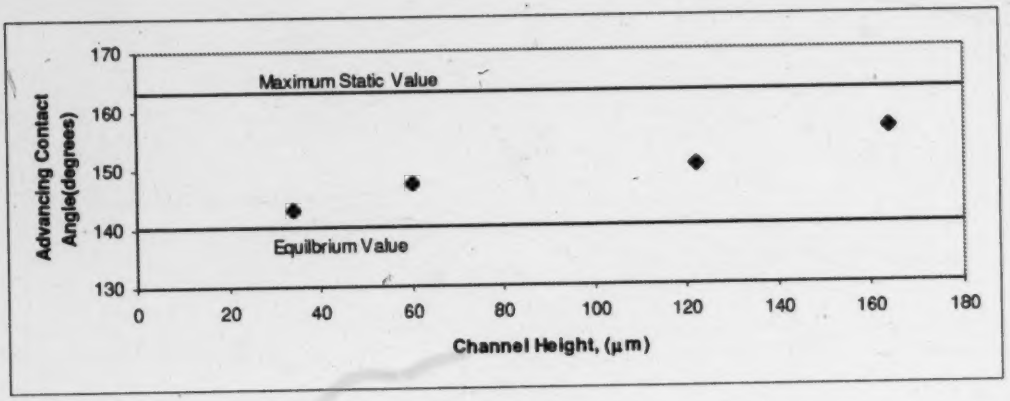

Figure 5.11 – Advancing contact angle versus channel height. Values plotted are those found by fitting the model predictions to the experimental data.

CHAPTER 6

SUMMARY AND FUTURE WORK

6.1 SUMMARY

The experimental results produced several identifiable trends:

1) Ca_{cr} will decrease as D_c increases for a specific channel height. The drag force on a bubble should increase with the bubble's contact diameter which explains this observation.
2) Ca_{cr} will decrease as h decreases. Several physical factors govern this observation. It was seen that the pressure gradient increase with decreasing h will be larger than the effects of decreasing surface area and decreasing flow velocity. The net effect is that the drag force of a bubble with contact diameter, D_c, will be larger in a smaller channel.
3) Ca_{cr} has decreasing dependence upon the ratio D_c/h as h decreases. This was shown to be due to the limited range of D_c that could be generated in the smaller channels.

The experimental data was shown to be very accurate for the measurements taken for h=164 μm and h=122 μm. Due to difficulties in generating small flow increments, the uncertainty for the h=60 μm and h=34 μm data is much larger.

A model was developed which performed well for much of the data tested. The model uses two formulations for drag force. The first is based upon the drag force

calculated from a simple pressure drop formulation. This method was shown to be an underestimate. The second method used the theoretical formulation for the drag force on a sphere in shear flow which was shown to be an overestimate. Combining the two drag force formulations results in a range for the drag force. The adhesion force was modeled with a dynamic contact angle hysteresis analysis. The receding contact angle was modeled using the method of Cox(1986). The advancing contact angle could not modeled this way due to the limitations of Cox's method. The advancing contact was used as a tuning factor to fit the model predictions to the model data. Equating the formulations for the drag force to the adhesion force allows the critical capillary number to be solved for. The model was shown to predict the critical state well. The advancing contact angles used to fit the model fell in a range which was acceptable from a physical point of view. All 'best fit' advancing contact angles fell between the equilibrium contact angle and the maximum static contact angle as expected.

6.2 FUTURE WORK

Experimentally, it would be useful to continue by examining the effects of changing the shearing fluid. This would allow comparison between the data of this study. In addition, if the oil viscosity is lowered sufficiently, the advancing contact angle would be able to be modeled with Cox's method. This would eliminate the need for a tuning factor in the adhesion force modeling.

The drag force formulation could be improved with a three dimensional computational fluid dynamics(CFD) simulation. Such a simulation would have to account for the complex shape of the bubble interface as it changes with the dynamic contact angle changes. Coupling Cox's method, the Laplace Equation of Capillarity, and the CFD solver would allow the drag force to determined very precisely. To simplify this work, the results of Chapter 4 could be used to approximate the bubble as a cylinder under certain combinations of D_c and h.

BIBLIOGRAPHY

Basu, S., Nandakumar, K., and Masliyah, J.H., *Journal of Colloid and Interface Science*, v.182 (1996) 82.

Basu, S., Nandakumar, K., and Masilyah, J.H., *Journal of Colloid and Interface Science*, v.190 (1997) 253.

Beckwith, T.G., Marangoni, R.D., and Lienhard V, J.H., *Mechanical Measurements, 5th Edition*, Addison-Wesley Publishing Company, 1993.

Callen, H.B., *Thermodynamics and an Introduction to Thermostatistics, 2nd Edition*, John Wiley & Sons, New York, 1985.

Cheng, P., Li, D., Boruvka, L., Rotenburg, Y., and Neumann, A.W., *Colloids Surfaces*, v.43, (1990) 151.

Cox, R.G., *Journal of Fluid Mechanics*, v.168 (1986) 169.

Goldman, A.J., Cox, R.G., and Brenner, H., *Chemical Engineering Science*, v.22 (1967) 637.

Gu, Y., and Li, D., *Internal Report to Imperial Oil*, 1996.

Gu, Y., and Li, D., *Journal of Chemical Engineering of Japan*, v.30 (1997) 302.

Gu, Y., and Li, D., *Colloids and Surfaces: Physicochemcial and Engineering Aspects*, v.142 (1998) 243.

Hoffman, R., *Journal of Colloid and Interface Science*, v.50 (1975) 228.

Incropera, F.P., and Dewitt, D.P., *Introduction to Heat Transfer, 3rd Edition*, John Wiley & Sons, Inc., 1996.

Jen, C.J., Li, H. -M., and Usami, S., *American Journal of Physiology*, v.270 (1996) 2.

Kuo, S.C., Hammer, D.A., and Lauffenburger, D.A., *Biophysical Journal*, v.73 (1997) 517.

Macdougall and Ockhert, *Proc. Roy. Soc.*, A180, (1942) 151.

Mahe, M., Vignes-Adler, M., and Adler, P.M., *Journal of Colloid and Interface Science*, v.126, (1988) 314.

Mahe, M., Vignes-Adler, M., and Adler, P.M., *Journal of Colloid and Interface Science*, v.126, (1988) 329.

Mahe, M., Vignes-Adler, M., and Adler, P.M., *Journal of Colloid and Interface Science*, v.126, (1988) 337.

Ngan, C.G., and Dussan, E.B.V., *Journal of Colloid and Interface Science*, v.50 (1975) 30.

Shames, I.H., *Mechanics of Fluids, 3rd Edition*, McGraw-Hill Inc., 1992.

Xia, Z., Goldsmith, H.L, and Van de Ven, T.G.M., *Biophysical Journal*, v.60, (1994) 1222.

APPENDIX A – COMPUTER PROGRAMS

Code 2.1 – Sum of Squares Minimization for a Circular Profile

```
program least
************************************************************************
*       Program fits a circle to a file of x,y coordinates.  The eqn
*       (y-a)^2 + (x-b)^2 = r^2 is used and the sum of squares is
*       minimized with respect to a,b,and r.
************************************************************************
      real a,b,r,sos,x(100),y(100),xmin,xmax,ymin,ymax
      real abest,bbest,rbest,best,temp
      integer i,j,n

* OPEN FILES, SET UP INITIAL GUESS FOR PARAMETERS
      open(8,file='bubble.txt',status='unknown')
      read(8,*)n
      xmin=10000
      ymin=10000
      xmax=-10000
      ymax=-10000

* READ IN COORDINATES AND FIND MINIMUM AND MAXIMUM VALUES FOR X&Y
      do 10 i=1,n
      read(8,*)y(i),x(i)
      if(x(i).lt.xmin) then
      xmin=x(i)
      endif
      if(x(i).gt.xmax) then
      xmax=x(i)
      endif
      if(y(i).lt.ymin) then
      ymin=y(i)
      endif
      if(y(i).gt.ymax) then
      ymax=y(i)
      endif
 10   continue
      close(8)

* USE MINMAX VALUES TO FIND INITIAL GUESSES FOR B AND R
      bbest=0.5*(ymin+ymax)
      rbest=0.5*(ymax-ymin+xmax-xmin)/2.0

* MINIMIZE 'A' KEEPING 'B' AND 'R' CONSTANT
      do 50 j=1,10
      best=1e12
      do 20 a=xmin,xmax,1
      call square(n,x,y,a,bbest,rbest,sos)
      if(sos.lt.best) then
      best=sos
      abest=a
      endif
 20   continue

* MINIMIZE 'B' KEEPING 'R' CONSTANT AND WITH OPTIMAL 'A'
      best=1e12
      do 21 b=ymin,ymax,1
      call square(n,x,y,abest,b,rbest,sos)
      if(sos.lt.best) then
      best=sos
      bbest=b
      endif
```

```
 21   continue

* MINIMIZE 'R' KEEPING OPTIMAL 'A' AND OPTIMAL 'B'
      best=1e12
      do 22 r=rbest-50,rbest+50,1
      call square(n,x,y,abest,bbest,r,sos)
      if(sos.lt.best) then
      best=sos
      rbest=r
      endif
 22   continue
 50   continue
      print *,'DIAMETER =',rbest*2,' pixels'
      end
*************************************************************************
*       Subroutine calculates error via sum of squares method.  The
error
*       is the distance from (x(i),y(i)) to the center of a circle
*       with equation (y-b)^2+(x-a)^2 = r^2
*************************************************************************
      subroutine square(n,x,y,a,b,r,sos)
      real a,b,r,sos,xerr,yerr,rot,x(100),y(100)
      integer i,n
      xerr=0.0
      yerr=0.0
      do 100 i=1,n
      rot=sqrt((x(i)-a)**2+(y(i)-b)**2)
      if(rot.ne.0) then
      rot=abs(rot-r)/rot
      xerr=xerr+(rot*abs(x(i)-a))**2
      yerr=yerr+(rot*abs(y(i)-b))**2
      else
      xerr=r**2
      yerr=r**2
      endif
 100  continue
      sos=xerr+yerr
      return
      end
```

Code 3.1 – Determine Contact Angles from 20 interface profile points near surface

```
program contact
************************************************************************
*     This program will calculate matrix coefficents for computing
*     contact angles if given bubble perimeter points and stopping pts.
************************************************************************
      real x(20),y(20),xs1,xs2,ys1,ys2,theta,angle
      integer i,xread,yread

* MANUALLY CHANGE THE FOLLOWING VALUES. THEY REPRESENT THE PIXEL COORD
* OF THE BUBBLE INTERFACE AT THE SOLID SURFACE
      xs1=148
      ys1=281
      xs2=160
      ys2=426

* COMPUTE THE ANGLE BETWEEN THE TWO POINTS AT THE SURFACE. ACCOUNTS FOR
* ANY TILTING OF THE IMAGE.
      if(xs1.eq.xs2) then
      angle=0.0
      else
      angle=atan2(xs2-xs1,ys2-ys1)
      endif

* FIND THE 20 POINTS NEAREST TO THE ADVANCING CONTACT ANGLE AND CALL
* THE CURVING FITTING AND ANALYSIS SUBROUTINE
      open(8,file='input.txt',status='unknown')
      do 10 i=1,20
      read (8,*)xread,yread
      x(i)=xread
      y(i)=yread
 10   continue
 11   call shift(x,y)
      read (8,*)x(20),y(20)
      if(x(20).eq.xs1.and.y(20).eq.ys1) then
      call compute(x,y,theta)
      goto 12
      endif
      goto 11
 12   print *,'Contact Angle #1 ',(theta+angle)*180.0/3.1415+90.0

* FOLLOW THE SAME PROCEDURE FOR THE 20 POINTS NEAREST THE RECEDING
* CONTACT ANGLE
      do 30 i=1,20
      read (8,*)xread,yread
      x(i)=xread
      y(i)=yread
 30   continue
 41   call shift(x,y)
      read (8,*)x(20),y(20)
      if(x(20).eq.xs2.and.y(20).eq.ys2) then
      call compute(x,y,theta)
      goto 42
      endif
      goto 41
 42   print *,'Contact Angle #2 ',(theta-angle)*180.0/3.1415+90.0
      end
************************************************************************
*     This subroutine shifts the data back one position in the xy array
************************************************************************
      subroutine shift(x,y)
```

```
      real x(20),y(20)
      integer i
      do 20 i=2,20
      x(i-1)=x(i)
      y(i-1)=y(i)
 20   continue
      return
      end
*************************************************************************
*     This subroutine calculates a quadratic best fit to the interface
*     profile.  Computing the slope of this curve at the contact surface
*     allows the contact angle to be found.
*************************************************************************
      subroutine compute(x,y,theta)
      real x(20),y(20),result(8),a,b,c,theta,slope
      double precision mat(3,4),temp
      integer i

      do 87 i=1,10
      result(i)=0.0
 87   continue
      result(1)=20.0
      do 88 i=1,20
      result(2)=result(2)+x(i)
      result(3)=result(3)+x(i)**2
      result(4)=result(4)+x(i)**3
      result(5)=result(5)+x(i)**4
      result(6)=result(6)+y(i)
      result(7)=result(7)+x(i)*y(i)
      result(8)=result(8)+x(i)**2*y(i)
 88   continue

      mat(1,1)=result(1)
      mat(1,2)=result(2)
      mat(1,3)=result(3)
      mat(1,4)=result(6)
      mat(2,1)=result(2)
      mat(2,2)=result(3)
      mat(2,3)=result(4)
      mat(2,4)=result(7)
      mat(3,1)=result(3)
      mat(3,2)=result(4)
      mat(3,3)=result(5)
      mat(3,4)=result(8)

* STANDARD GAUSSIAN ELIMINATION TO SOLVE FOR THE UNKNOWNS OF A 3X3
MATRIX
      temp=mat(1,1)
      do 110 i=1,4
      mat(1,i)=mat(1,i)/temp
 110  continue
      temp=mat(2,1)
      do 111 i=1,4
      mat(2,i)=mat(2,i)-mat(1,i)*temp
 111  continue
      temp=mat(3,1)
      do 112 i=1,4
      mat(3,i)=mat(3,i)-mat(1,i)*temp
 112  continue
      temp=mat(2,2)
      do 113 i=1,4
      mat(2,i)=mat(2,i)/temp
 113  continue
      temp=mat(3,2)
```

```
      do 114 i=1,4
      mat(3,i)=mat(3,i)-mat(2,i)*temp
 114  continue
      temp=mat(3,3)
      do 115 i=1,4
      mat(3,i)=mat(3,i)/temp
 115  continue

* THE SOLUTION IS: AX^2 + BX + C
      a=mat(3,4)
      b=mat(2,4)-a*mat(2,3)
      c=mat(1,4)-a*mat(1,3)-b*mat(1,2)

* THE DERIVATIVE IS: 2AX + B
      slope=2.0*a*x(20)+b
      theta=atan(abs(slope))

      return
      end
```

Code 5.1 – Evaluation of Cox's method using Simpson's method of integration

```
program simpson
*************************************************************************
      real L,deltax,sum,theta,beta,eval,f(1000),pi
      integer n,i

* SET UP PROBLEM
      L=16800.0
      pi=3.141592654
      n=1000
      open(8,file='output.txt',status='unknown')

      do 40 theta=1.0*3.1415/1000.0,3.1415,3.1415/1000.0
      deltax=theta/n
      sum=0.0

* FOLLOW SIMPSON'S INTEGRATION ALGORITHM WITH 1000 FUNCTION EVALUATIONS
      do 10 i=1,n
      beta=theta/n*i
      call func(L,beta,eval,pi)
      f(i)=eval
 10   continue
      sum=f(1)+f(n)
      do 20 i=2,n-1,2
      sum=sum+4.0*f(i)
      sum=sum+2.0*f(i+1)
 20   continue
      sum=sum*deltax/3.0
      write(8,*)theta,sum

 40   continue
      end
*************************************************************************
*This subroutine evaluates the function 1/f(theta) in Cox's method
*************************************************************************
      subroutine func(L,beta,eval,pi)
      real L,beta,eval,num,dem

      num=L**2*(beta**2-(sin(beta))**2)
      num=num+2*L*(beta*(pi-beta)+(sin(beta))**2)
      num=num+(pi-beta)**2-(sin(beta))**2
      num=num*2*sin(beta)
      dem=L*(beta**2-(sin(beta))**2)
      dem=dem*((pi-beta)+sin(beta)*cos(beta))
      dem=dem+((pi-beta)**2-(sin(beta))**2)*(beta-sin(beta)*cos(beta))
      eval=dem/num
      return
      end
```

Code 5.2 – Solving for Critical State in an iterative fashion.

```
program capillar

      double precision fa,ca,one,two,three,d,h,delta,deltaa,deltar
      double precision temp,error,a,yp,den,litr,height(4)
      real rx,ry,gof,tr,ad
      integer n,k


      integer i

      open (9,file='output.txt',status='unknown')

      height(1)=34e-6
      height(2)=60e-6
      height(3)=122e-6
      height(4)=164e-6

* START LOOPS THROUGH H AND D
      do 32 i=1,4
      h=height(i)
      do 10 d=2*h,20*h,h

* INITIAL GUESS FOR CA
      ca=0.001
      orig=ca

* USE COX'S METHOD TO OBTAIN RECEDING ANGLE FOR THIS CA AND H
 37   call ggof(0.6981,gof)
      gof=gof+ca*log(h/1e-6)
      call gtheta(tr,gof)
      tr=3.1415927-tr

* THIS SECTION IS WHERE THE ADVANCING CONTACT ANGLE IS GUESSED
      if(i.eq.1) then
      ad=2.495
      endif
      if(i.eq.2) then
      ad=2.57
      endif
      if(i.eq.3) then
      ad=2.625
      endif
      if(i.eq.4) then
       ad=2.73
      endif

* COMPUTE THE ADHESION FORCE
      fa=(cos(tr)-cos(ad))

* CALL LAPLACE SUB TO COMPUTE NECESSARY ADDITIONS TO D
      call laplace(d,h,ad,deltaa)
      call laplace(d,h,tr,deltar)
      delta=deltaa+deltar


* COMPUTE CA..TO SET FOR DRAG FORCE ONE, CHANGE THE LAST '2.0' TO A
*'1.0'
      ca=2.0/(7.65225*3.1415)/(((d+delta))**2)*d*h*fa*2.0

      if(abs(ca-orig).gt.1e-7) then
      orig=ca
      goto 37
```

```
      endif

      write(9,*)d/h,1000*ca,h

 10   continue
 32   continue

      close(9)
      end
*************************************************************************
*This subroutine solves the laplace equation of capillarity to find the
*largest deviation from a vertical interface assumption
*************************************************************************
      subroutine laplace(d,h,angle,delta)
      double precision d,h,radius,g,dx,gamma,rho,delta
      double precision y(500),ynot(500),forw,den
      real angle

      radius=d/2.0
      g=9.81
      dx=h/501.0
      gamma=0.03
      rho=879.2-1.2

      litr=((tan(angle-1.570796))**(-2)+1.0)*h*h/4.0


* SET UP INITIAL GUESS AS A CIRCULAR PROFILE
      do 91 n=1,500
      y(n)=radius+(litr-((n-1)*dx-h/2.0)**2)**0.5-h/2.0/tan(angle-
     &1.570796)
      ynot(n)=y(n)
 91   continue

* SET UP BOUNDARY CONDITIONS
      y(1)=radius
      ynot(1)=radius
      y(500)=radius
      ynot(500)=radius
 92   temp=0.0

      do 93 n=1,500
      temp=temp+y(n)-radius
      ynot(n)=y(n)
 93   continue

      forw=(2.0*y(1)-5.0*y(2)+4.0*y(3)-y(4))/(dx**2.0)

      do 20 n=2,499

      x=(n-1)*dx
      yp=(y(n+1)-y(n-1))/2.0/dx
      den=(1.0+(tan(angle-3.1415/2.0))**2)

      a=forw*den**(1.5)+tan(angle3.1415/2.0)*den**(0.5)/radius+rho*g*x/
      &amma
      a=a-yp/y(n)/((1+yp**2)**0.5)
      a=a*(1.0+yp**2)**(1.5)
      y(n)=0.5*(y(n+1)+y(n-1)-a*(dx**2))
 20   continue

* OVER-RELAXATION IMPLEMENTATION
      do 44 n=1,500
      y(n)=ynot(n)+1.5*(y(n)-ynot(n))
```

```
 44   continue

      error=0.0
      do 12 n=1,500
      error=error+y(n)-radius
 12   continue
      error=abs((error-temp)/(error))


      if(error.gt.1e-5) then
        goto 92
      endif

*  DETERMINE LARGEST DEVIATION FROM CONVERGED PROFILE
      call bigges(y,delta)
      delta=delta-radius

      return
      end
*******************************************************************************
*This subroutine finds the largest deviation from a converged profile
*******************************************************************************
      subroutine bigges(y,delta)
      double precision y(500),delta
      integer q

      delta=0.0
      do 109 q=1,500
      if(y(q).gt.delta) then
      delta=y(q)
      endif
 109  continue
      return
      end
*******************************************************************************
*This subroutine returns the value of g(theta) given theta
*for the receding contact angle solution of Cox's method
*******************************************************************************
      subroutine ggof(alpha,gof)
      real alpha,gof,beta(2),func(2),per
      integer i

      open (8,file='gtheta.txt',status='unknown')
      read(8,*)beta(1),func(1)
 99   read(8,*)beta(2),func(2)
      if(alpha.le.beta(2).and.alpha.gt.beta(1)) then
      per=(alpha-beta(1))/(beta(2)-beta(1))
      gof=func(1)+per*(func(2)-func(1))
      else
      beta(1)=beta(2)
      func(1)=func(2)
      goto 99
      endif
      close(8)
      return
      end
*******************************************************************************
*This subroutine returns theta given g(theta) for the receding
*contact angle solution to Cox's method
*******************************************************************************
      subroutine gtheta(alpha,gof)
      real alpha,gof,beta(2),func(2),per
      integer i
      open (8,file='gtheta.txt',status='unknown')
```

```
      read(8,*)beta(1),func(1)
599   read(8,*)beta(2),func(2)
      if(gof.le.func(2).and.gof.gt.func(1)) then
      per=(gof-func(1))/(func(2)-func(1))
      alpha=beta(1)+per*(beta(2)-beta(1))
      else
      beta(1)=beta(2)
      func(1)=func(2)
      goto 599
      endif
      close(8)
      return
      end
```